MAPPING PERCENT TREE MORTALITY DUE TO DROUGHT IN PIÑON-JUNIPER

WOODLANDS USING A LANDSAT TIME SERIES FROM NORTHERN NEW MEXICO

A Thesis

Presented in Partial Fulfillment of the Requirements for the

Degree of Master of Science

with a

Major in Geography

in the

College of Graduate Studies

University of Idaho

by

Seth Richard Gorelik

B.S., University of California, Santa Barbara, 2012

Major Professor: Jeffrey A. Hicke, Ph.D.

Committee Members: Arjan J.H. Meddens, Ph.D.; Crystal A. Kolden, Ph.D.

Department Administrator: Leslie L. Baker, Ph.D.

December 2017

Authorization to Submit Thesis

This thesis of Seth Richard Gorelik, submitted for the degree of Master of Science with a major in Geography and titled "Mapping Percent Tree Mortality Due to Drought in Piñon-Juniper Woodlands Using a Landsat Time Series from Northern New Mexico," has been reviewed in final form. Permission, as indicated by the signatures and dates given below, is now granted to submit final copies to the College of Graduate Studies for approval.

Major Professor: _____ Date: _____
                            Jeffrey A. Hicke, Ph.D.

Committee Members: _____ Date: _____
                            Arjan J.H. Meddens, Ph.D.

_____ Date: _____
                            Crystal A. Kolden, Ph.D.

Department
Administrator: _____ Date: _____
                            Leslie L. Baker, Ph.D.

Abstract

In the early 2000s, severe drought and beetle outbreaks brought on by climate change led to extensive piñon pine mortality in northern New Mexico. Mapping piñon mortality is critical for understanding and monitoring impacts to ecosystem services. I used Landsat imagery, finer-resolution reference data, and statistical modeling to predict absolute within-pixel percent tree mortality (PTM). I found that a balanced random forest model had the highest accuracy. I applied the model to a time series and assessed spatial and temporal patterns of the estimated tree mortality. Pixels within the study area experienced a mean of 42.3% tree mortality, a mean duration of 3 years, and a mean rate of mortality of 22% per year. From 1987 to 2009, cumulative tree mortality reached 67,190 ha, or 19.8% of the woodland area, the equivalent of 48.9 million piñons. These results demonstrate the capability of mapping drought-induced PTM using a Landsat time series.

Acknowledgements

To my parents, siblings, and Lauren,

thank you for your support.

Table of Contents

List of Figures

List of Tables

List of Equations

1. Introduction

Extensive tree mortality has occurred globally in recent years due to a warming climate (Breshears et al., 2005; Allen et al., 2010). Climate change increases many forests' vulnerability to ecosystem changes and tree mortality via drought and other disturbances (Melillo et al., 2014). Such mortality reduces the ability for forests to deliver ecosystem goods and services (e.g., timber, recreation, wildlife habitat, and carbon sequestration), impacts biodiversity, and interacts with other forest disturbances such as insects or fire (e.g., Clifford et al., 2008; Breshears et al., 2011; Hicke et al., 2012*a*, 2012*b*; Anderegg et al., 2012; IPCC, 2014*b*; Hurteau et al., 2014). In the early 2000s, the southwestern United States experienced widespread mortality of two-needle (*Pinus edulis* Engelmann) and single-leaf (*Pinus monophylla* Torrey and Fremont) piñon pines due to drought and bark beetle outbreaks (Breshears et al., 2005; Williams et al., 2012). The combination of attributed conditions (i.e., low water availability, high temperatures, and high vapor pressure deficit) has been termed a "global-change-type" drought (Breshears et al., 2005) and is predicted to continue or increase in the next century resulting in regional-scale tree mortality of dominant vegetation (Allen, 2007; Williams et al., 2012; IPCC, 2014*b*).

Despite the significance of tree mortality, there remains limited quantitative information available about the spatial and temporal characteristics of climate-related mortality in woodland ecosystems (Allen et al., 2010; Hansen et al., 2013). For example, many maps of mortality only document location of die-offs, not severity, extent, or timing (Allen et al., 2010). Past research has utilized satellite remote sensing to quantify extent and patterns of die-off (Coops et al., 2006; Huang et al., 2010; Meddens et al., 2011; Garrity et al., 2013; Krofcheck et al., 2014), yet the majority of this research has focused on assessing methods to produce categorical classifications of mortality in dense- or closed-canopy forests. Recent studies in closed-canopy forests have demonstrated that Landsat data can be used to predict continuous mortality within a 30-m pixel as opposed to a categorical classification,

providing a more sensitive representation of mortality (Meigs et al., 2011; Meddens and Hicke, 2014).

In contrast to these forests, however, open canopies characterize semi-arid woodlands. Thus, soils and understory contribute more to the spectral reflectance, making changes in vegetation (i.e., mortality) a distinct challenge to detect with satellite-based remote sensing in these areas (e.g., Huang et al., 2010; Krofcheck et al., 2014; Schwantes et al., 2016). Furthermore, when there is low mortality (i.e., few trees die within a given satellite pixel) in open-canopy woodlands, the challenge of detecting its spectral signal becomes more problematic. Past studies have demonstrated the capability of very high-resolution imagery (e.g., QuickBird) to map tree mortality in these landscapes (e.g., Garrity et al., 2013). However, such imagery has limited spatial and temporal coverage and is costly. Providing spatiotemporal information about tree mortality in woodlands is necessary for understanding the influences of climate change on these forests as well as assessing impacts to ecosystem services (Allen et al., 2010; McDowell, 2011). Moderate-resolution (e.g., Landsat) imagery balances the requirements of large spatial extents, substantial archival imagery, low cost (i.e., free) user acquisition, and the spatial resolution needed to detect tree mortality in open-canopy woodlands.

1.1.   Climate change, drought, and tree mortality in the Southwest

While piñon pines can form pure stands, they are commonly known to intermix with one or more juniper species, forming the coniferous piñon-juniper (PJ) woodland, one of the most widespread plant communities in the United States (Lanner, 1981; Gottfried et al., 1995; Allen et al., 1998). It is estimated that there is up to 30 million ha of PJ woodland within the United States (Lanner, 1981; Gottfried et al., 1995; Ferguson, 2006). The semi-arid PJ woodland is an open forest of low and often bushy or contorted trees and shrubs (Lanner, 1981). The two-needle piñon, also known as the "common" or "Colorado" piñon, is the most common piñon species found in the PJ woodland of New Mexico (Dick-Peddie, 1993). It

Figure 1.1. Piñon mortality along Interstate 25, south of Santa Fe, NM in April, 2003 (photo by Bob Heuer).

produces commercial piñon pine nuts (Lanner, 1981; Breshears et al., 2011). The one-seed juniper (*Juniperus monosperma* Engelmann) is the most common juniper species in New Mexico; however, in northern New Mexico, it may share dominance with Rocky Mountain juniper (*Juniperus scopulorum*), and additionally the Utah juniper (*Juniperus osteosperma*) in the northwest corner of the state (Dick-Peddie, 1993). While piñon and juniper tree species generally require the least amount of available moisture of all conifers (Dick-Peddie, 1993), junipers are the more drought tolerant of the two and tend to dominate drier sites (Gottfried et al., 1995). Likewise, the proportion of piñons found in a PJ woodland will tend to increase with an increase in elevation and available moisture (Gottfried et al., 1995).

In the early 2000s, more than 50% of the contiguous United States experienced moderate to severe drought conditions (Lawrimore and Stephens, 2003). In particular, the southwestern United States experienced rapid, widespread mortality of two-needle and single-leaf piñon pines due to drought and piñon ips (*Ips confusus* Leconte) outbreaks between 2002 and 2004 (Breshears et al., 2005; Williams et al., 2012; Meddens et al., 2015) (Figure 1.1). While the severe drought of the early 2000s had slightly greater total precipitation than a previous sub-continental drought in the 1950s, which had induced

notable *Pinus ponderosa* mortality within the region (Allen and Breshears, 1998), the more recent multi-year drought was considerably warmer and the resulting mortality was subsequently greater in magnitude and extent (Breshears et al., 2005). The low water availability, high temperatures, and high vapor pressure deficit in the region during the early 2000s drought, since termed a "global-change-type" drought (Breshears et al., 2005, 2009), led to an increase in stands of stressed trees, allowing for ips populations to erupt (Raffa et al., 2008; Gaylord et al., 2013). Unlike some other bark beetle species, piñon ips do not kill healthy trees (Hicke and Zeppel, 2013). Therefore, after the severe drought, the local supply of stressed trees declined, followed by a sharp decline in ips populations (Raffa et al., 2008). In a review of 21 observational studies of piñon mortality in the American Southwest by Meddens et al. (2015), bark beetle outbreaks were cited as a contributing factor of the mortality and drought was reported as the main factor.

Drought is a phenomenon in which its onset and end are often hard to identify other than retrospectively (Wilhite and Glantz, 1985). Drought is considered a serious hazard with the potential for numerous environmental and socioeconomic impacts (Wilhite and Buchanan-Smith, 2005; NOAA, 2016). Within the United States, annual economic losses from drought total nearly \$9 billion per year, ranking it second in types of phenomena associated with billion-dollar weather disasters during the past three decades (NOAA, 2016). Often definitions of drought vary across studies and disciplines, yet they commonly refer to a deficiency of precipitation within a region resulting in a water shortage necessary for some activity such as plant growth or clean drinking water (Wilhite and Glantz, 1985; Hanson and Weltzin, 2000; Redmond, 2002). As a forest disturbance, drought can occur broadly and typically with no single starting location (unlike fire, insects, or pathogens). Throughout western North America, drought and warming atmospheric temperatures have induced extensive insect outbreaks and mortality across a range of forest types, affecting 20 million ha of forest and many tree species since 1997 from Mexico to Alaska (Raffa et al., 2008; Allen et al., 2010; Bentz et al., 2010). Given that forests and shrublands combined make up

46% of land cover within the conterminous United States (Homer et al., 2015), the projected increases in frequency and intensity in drought within some regions have raised concern about potential impacts to terrestrial ecosystem productivity, biogeochemical cycling, and the availability of water resources (Hanson and Weltzin, 2000; Melillo et al., 2014).

While the exact mechanisms of drought-induced tree mortality are not well understood, there are two interdependent mechanisms through which it is hypothesized to occur: hydraulic failure and carbon starvation (Meddens et al., 2015). Hydraulic failure can occur when reduced soil water supply combined with high evaporative demand results in cavitation of water conduits within the xylem, obstructing the transportation of water and dehydrating the plant (McDowell et al., 2008). Carbon starvation can occur from prolonged water stress as well, but in this case a plant will close its stomata to prevent hydraulic failure (McDowell et al., 2008). This avoidance of hydraulic failure also results in decreased photosynthetic uptake of carbon, and because there remains a continued demand for the metabolism of carbohydrates for survival, the plant will subsequently starve (McDowell et al., 2008; McDowell, 2011). During drought, tree mortality can result from a variable combination of hydraulic failure and carbon starvation depending on the conditions of the drought (McDowell et al., 2011; Sevanto et al., 2014). Species or plant communities existing at the margin of their suitable habitat range may experience particularly severe effects (Dale et al., 2001). Furthermore, multiple (often interrelated) factors associated with climate (e.g., temperature, precipitation), terrain (e.g., topography), vegetation (e.g., stand structure), and biotic agents (e.g., bark beetles) may lead to either hydraulic failure or carbon starvation, or both, resulting in mortality (Meddens et al., 2015). In particular, it is thought that beetles amplified piñon pine mortality from the early 2000s drought within the Southwest (Shaw et al., 2005; Raffa et al., 2008). Understanding the precise contributions of mechanisms underlying mortality remain a knowledge gap for the accurate prediction of timing and location of vegetation change under future climate projections (McDowell et al., 2011; Anderegg et al., 2015).

The global climate is changing and it is largely attributed to anthropogenic forcings (Oreskes, 2004; IPCC, 2014*b*; Melillo et al., 2014). Emissions of greenhouse gases have risen since the pre-industrial era, primarily due to the burning of fossil fuels and deforestation (Karl et al., 2009; IPCC, 2014*a*; Melillo et al., 2014). A climate suitable for sustaining life on Earth is dependent on the functioning of a natural greenhouse effect, which is the warming that results when certain gases in the atmosphere (i.e., greenhouse gases) such as water vapor, nitrous oxide, methane, and carbon dioxide trap heat that radiates from Earth toward space (Karl et al., 2009). However, human activities that release additional greenhouse gases have intensified the natural greenhouse effect (Karl et al., 2009). Relative to pre-industrial levels, global carbon dioxide emissions have increased by about 40%, nitrous oxide has increased by about 20%, and methane has increased by about 250% (Melillo et al., 2014). In the United States, average temperatures have increased by 1.1 °C since the start of the instrumental record–with most of the increase occurring within the past 50 years–and are projected to increase an additional 1.1-2.2 °C over the next few decades (Melillo et al., 2014). Over the next century, global temperatures are projected to rise by 1.6-2.8 °C under a low emissions scenario and 2.8-5.6 °C under a high emissions scenario (IPCC, 2014*a*).

Rises in temperatures have already led and will continue to lead to more intense and frequent extreme climate and weather events such as heat waves, hurricanes, storms, floods, and drought (Melillo et al., 2014). Often these extreme events are the primary way through which people experience impacts of climate change (Melillo et al., 2014). While natural disturbance, by itself, is not always a negative impact to forests (Perry et al., 2008), it is thought that with human-induced climate change, forests become more vulnerable to mortality via rapid alterations in the timing, intensity, frequency, and extent of both abiotic (e.g., drought, fire) and biotic (e.g., insects) disturbances (Melillo et al., 2014; Allen et al., 2015). A changing climate has the potential to alter landscapes through species migration on decadal to millennial timescales; however, widespread tree mortality events can drastically transform the structure and function of ecosystems at the regional scale on a sub-decadal

timescale (McDowell et al., 2008). Trees grow slowly, taking up to hundreds of years to mature, and they can be killed by drought relatively fast (i.e., several months or years) (Allen et al., 2010).

Tree mortality reduces the ability for forests to deliver ecosystem goods and services such as carbon storage, biodiversity, wildlife habitat, timber yield, soil microbial community activity, and water quality (e.g., Breshears et al., 2011; Hicke et al., 2012a, 2012b; Anderegg et al., 2012; IPCC, 2014b; Hurteau et al., 2014; Warnock et al., 2016). For example, it is estimated that the 2000s drought accompanied by insect and disease outbreak in the Southwest PJ woodlands is responsible for 5 Tg C of live aboveground woody biomass loss (Huang et al., 2010). Additionally, several bird species such as the screech owl (*Otus asio*), gray flycatcher (*Empidonax wrightii*), and the plain titmouse (*Parus inornatus*) are known to only breed within piñon-juniper habitats (Gottfried et al., 1995). Furthermore, the piñon pine is the iconic state tree of New Mexico and its mortality within the region bears cultural significance (Breshears et al., 2011). Severe droughts such as the one in the early 2000s across the southwestern United States are predicted to continue or increase in the next century likely resulting in further regional-scale mortality of dominant vegetation (Allen, 2007; Williams et al., 2012; IPCC, 2014b; McDowell et al., 2015b).

1.2. Remote sensing of tree mortality

Satellite and airborne remote sensing provides the ability for unobtrusive, objective, systematic, and repeatable observations of changes in landscape patterns across broad temporal and spatial scales (Jensen, 2007). The usefulness of remote sensing in studying climate-related forest mortality is widely recognized (e.g., Coops et al., 2006; Hicke and Logan, 2009; Huang et al., 2010; Meddens et al., 2011, 2013; Bright et al., 2012; Clifford et al., 2013; Zhang et al., 2013; Garrity et al., 2013; Hansen et al., 2013; Meddens and Hicke, 2014; Krofcheck et al., 2014; Hartmann et al., 2015; McDowell et al., 2015a). There are multiple satellite platforms and optical sensors that can be used to monitor mortality

resulting from widespread drought events (Jensen 2007, Zhang et al. 2013). The choice of satellite sensor is critical, because it determines the spatial extent and spatial detail that can be measured on the ground (Figure 1.2). The broader the spatial extent a sensor can record, the coarser the spatial detail of the imagery.

The detectability of forest disturbances from remotely sensed imagery is determined by a balance of spatial, temporal, and spectral characteristics both of the disturbance and the imagery (Wulder et al., 2006). For example, monitoring forest die-off on the Earth's surface over large spatiotemporal scales can be accomplished with remotely sensed data that is acquired systematically, globally, and made freely available, such as with the Landsat series of satellites (Hansen et al., 2013). Landsat imagery cover broad spatial extents, often provide spatial detail sufficient for mapping trees, and have a long archival record. Hansen et al. (2013) demonstrated the potential for monitoring forest dynamics (i.e., canopy cover loss) globally using Landsat imagery, but did not separate disturbance types (e.g., drought). Disturbance events often result in varying levels of mortality severity (defined here as percent of tree mortality per area).

While past studies have utilized remote sensing to quantify extent and patterns of climate-induced forest die-offs, the majority of this research has focused on assessing methods to produce categorical classifications of mortality in dense- or closed-canopy forests (e.g., Meddens et al., 2011, 2013; Hart and Veblen, 2015). Few studies have used Landsat data in these forests to detect continuous proportions (i.e., percentages) of mortality within 30-m pixels as opposed to a categorical classification, providing a more sensitive detection of mortality severity (e.g., Meigs et al., 2011; Meddens and Hicke, 2014; Long and Lawrence, 2016). Fewer studies have assessed Landsat-based methods in open-canopy woodlands for detecting continuous proportions of tree mortality (e.g., Ferguson, 2006; Huang et al., 2010; Schwantes et al., 2016). Huang et al. (2010), for example, used Landsat imagery to map mortality and calculated subsequent biomass loss within the PJ woodlands of southern Colorado resulting from multi-year drought. However, their work required field
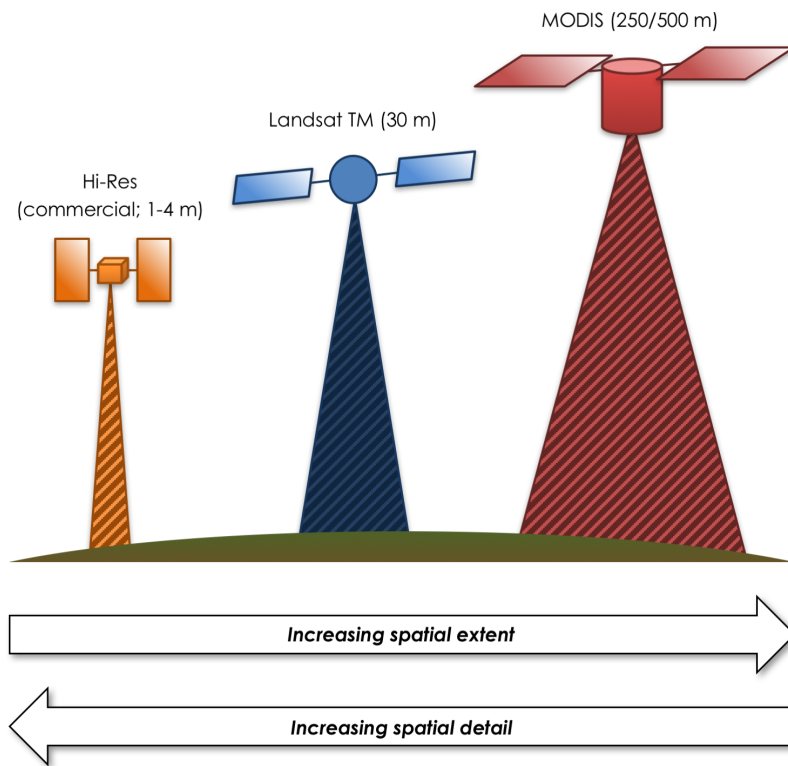
Figure 1.2. Types of satellite data used in remote sensing studies of tree mortality. Adapted from Meddens et al. (2009).

measurements of aboveground biomass for model development and evaluation. In addition, they used SMA to detect sub-pixel proportions of piñon mortality and acknowledged that challenges remain for more accurately unmixing herbaceous and woody vegetation cover (Huang et al., 2010). Garrity et al. (2013) mapped drought-induced piñon mortality within the PJ woodland of northern New Mexico, but focused on a small area and produced a categorical classification using very fine resolution (0.6-m), commercial (expensive) imagery. Furthermore, Meddens et al. (2016) developed remote sensing methods for detecting land cover changes using Garrity et al.'s (2013) fine-resolution classifications of mortality in 2006 and 2011, but focused on forest recovery rather than mortality and did not scale up to 30-m Landsat resolution to estimates continuous proportions over a broad spatial range.

To statistically model continuous proportions restricted to the closed interval [0, 1], such as percent tree mortality within a 30-m Landsat pixel, ordinary least squares (linear)

regression is not an optimal approach, because it can return values for the predicted response variable that exceed the conceptual lower and upper bounds of zero and one, respectively (Ferrari and Cribari-Neto, 2004; Savage et al., 2015). For example, Meddens and Hicke (2014) modeled percent tree mortality within 30-m grid cells using linear regression, but then required percent tree mortality predictions of <0% or >100% be set to 0% and 100%, respectively. In addition, Ferguson (2006) mapped percent mortality in the PJ woodlands of northern New Mexico during the 2000s drought using high-resolution QuickBird imagery to train a Landsat (4 year) time series. He tested two separate multiple linear regression models; both of which resulted in limited predictive capability ($R^2 \leq 0.47$). Moreover, linear regression models assume a normal distribution of model residuals, typically violated by zero-inflated datasets, and therefore are not suitable for application to datasets that are zero-inflated. Modeling percent tree mortality in open-canopy woodlands with moderate or coarse resolution imagery likely involves working with zero-inflated data because (a) there can be many pixels with little to no canopy cover and/or (b) of the pixels within the data that do contain canopy cover, many of them might not experience disturbance resulting in mortality. Therefore, alternative modeling approaches are needed that are appropriate for zero-inflated continuous data such as Landsat-derived within-pixel percentages of tree mortality.

Beta regression has been applied in forestry applications (e.g., Korhonen et al., 2007; Eskelson et al., 2011; Wing et al., 2012), but few in combination with satellite imagery to map within-pixel percent live and/or dead canopy cover (e.g., Coulston et al., 2012; Long and Lawrence, 2016). Only one study (Schwantes et al., 2016) has assessed the use of zero-inflated beta (ZIB; Ospina and Ferrari, 2010, 2012) regression in combination with Landsat imagery to detect within-pixel percent tree mortality due to drought for open-canopy woodlands. Schwantes et al. (2016) used Landsat imagery from before and after a severe drought in 2011 to map and quantify mortality within woodlands across the state of Texas. To do so, they first created fine-scale (1-m) canopy loss maps by classifying orthophotos from the U.S.

National Agriculture Imagery Program (NAIP), validated with ground observations. Using the fine-scale canopy loss maps and coarser scale Landsat imagery (in addition to auxiliary explanatory variables), they built and evaluated two sets of models: 1) random forest and 2) zero-inflated beta (ZIB) regression. These models were then used to estimate continuous proportions of post-drought mortality across the study area. To account for misalignment between the orthophotos and the Landsat imagery, the estimations were aggregated to a spatial resolution of 60 m. Schwantes et al. (2016) found that the ZIB regression modeling yielded the highest accuracy for detecting drought-induced mortality within the open-canopy woodlands of Texas, which are dominated by junipers, oaks, elms, and honey mesquite trees. Their methods are novel in that ZIB regression together with satellite imagery had not previously been used, to the best of my knowledge, to map continuous proportions of mortality in woodlands. However, these methods have yet to be applied to produce a time series of percent tree mortality maps at a 30-m spatial resolution within the PJ woodlands of northern New Mexico for the early 2000s drought.

In open-canopy woodland ecosystems, there is a need to develop remote sensing methods that balance the requirements of utilizing imagery with fine spatial resolution (to detect mortality), broad spatial coverage, decades of archived records, and low- to no-cost to the user. Moderate-resolution Landsat imagery has the potential to balance these requirements for detecting and monitoring climate-related tree mortality within these ecosystems (e.g., Schwantes et al., 2016). In addition, no method for detecting tree mortality across all forest types at the global scale is currently available, yet such an algorithm is highly desirable given the importance of understanding at which spatiotemporal scales these disturbances occur and the drivers behind them (McDowell et al. 2015a). This research contributes directly to one component of such efforts: an algorithm for mapping a continuous measure (percentage) of drought-induced mortality at the 30-m spatial resolution in open-canopy woodlands. Furthermore, documenting the severity and timing of mortality in woodlands provides a baseline for further work to understand the influences of climate

change on these forests and assess impacts to ecosystem services (Allen et al., 2010; McDowell, 2011; McDowell et al., 2015a).

The overarching goals for this research are to (a) improve methods for mapping and quantifying drought-induced tree mortality in semi-arid regions using readily available, remotely sensed data, and (b) provide maps containing information about the timing, extent, and severity of tree mortality within the piñon-juniper woodlands related to the early 2000s drought in support of subsequent ecological analyses. Thus, the specific objectives of this research were to (1) develop and evaluate statistical models for estimating a continuous measure (percent) of tree mortality due to drought within the open-canopy piñon-juniper woodlands of northern New Mexico at the 30-m spatial resolution, using (a) Landsat imagery and (b) finer-resolution reference data, (2) produce a time series of percent tree mortality maps by applying the optimal statistical model from Objective 1 (developed within the region of the reference image) to the entire time series of Landsat imagery, and (3) document spatial and temporal patterns within the time series of drought-induced tree mortality.

2. Methods

2.1. Study area

The study area is located in northwest New Mexico in the foothills of the southern Rocky Mountains and spans the spatial extent of Path 34, Row 35 of the Worldwide Reference System-2 (Figure 2.1). This study area was chosen for several reasons. First, a global-change-type drought occurred in this region in the early 2000s (Breshears et al., 2005; Allen, 2007), causing widespread forest mortality and killing up to 350 million piñon pines
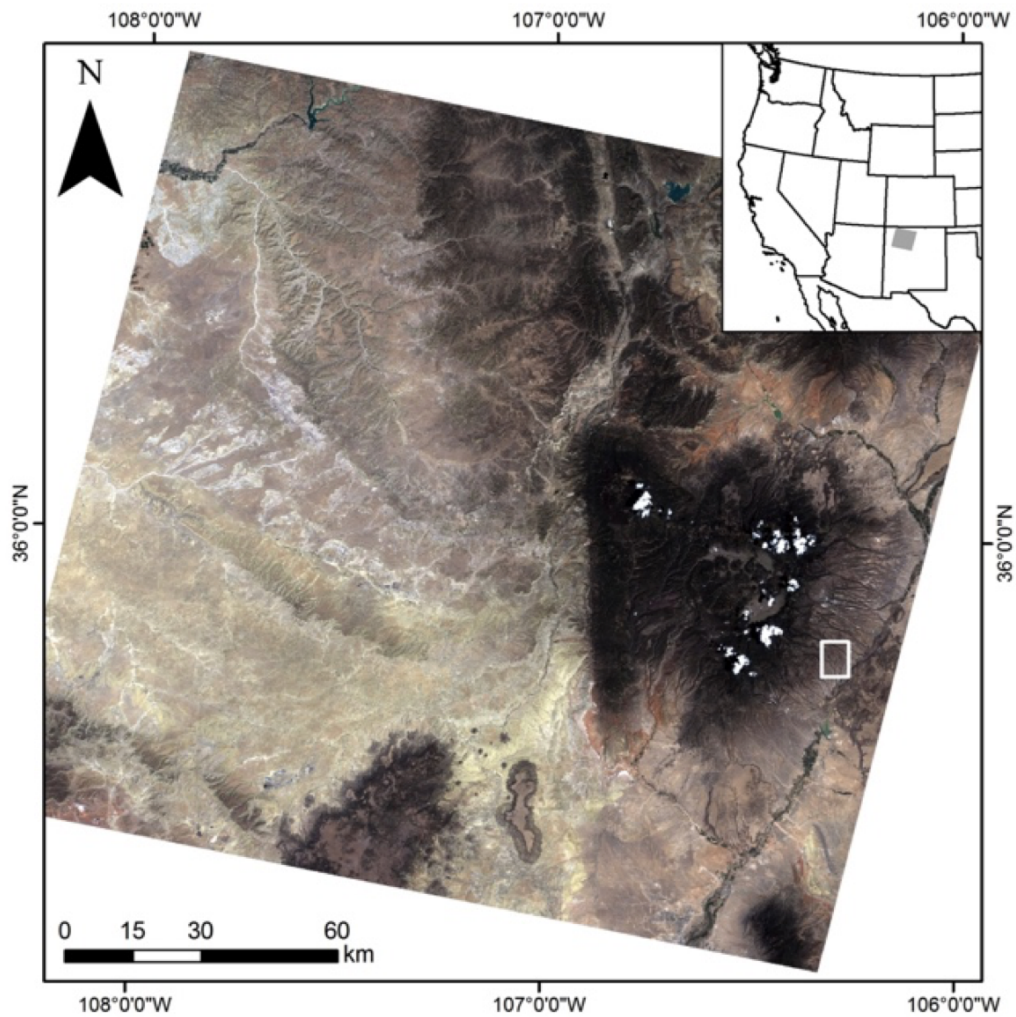
Figure 2.1. Study area location in the western United States (upper right; gray polygon) and true color Landsat path 34, row 35 image from July 4, 2003. The white rectangle within the Landsat scene indicates the location of the reference data used for model development and evaluation.

(Meddens et al., 2012; Hicke and Zeppel, 2013). Second, a variety of forest disturbances have been documented in this area, including wildfire, drought, bark beetles, and insect defoliators (e.g., Allen and Breshears, 1998; Breshears et al., 2005; Allen, 2007; McDowell et al., 2008), thereby providing information to assist with attributing observed mortality. Third, this study is based on prior research within this region by two scientists, Drs. Steven Garrity (formerly of Los Alamos National Laboratory) and Arjan Meddens (University of Idaho), who have since moved to other projects, but have provided valuable data sets and publications (e.g., Garrity et al., 2013). Fourth, the Hicke Lab at the University of Idaho has existing collaborations with scientists who have extensive field (i.e., Dr. Craig Allen, USGS; Brian Jacobs, formally of NPS) and remote sensing (i.e., Dr. Meddens) experience in this region.
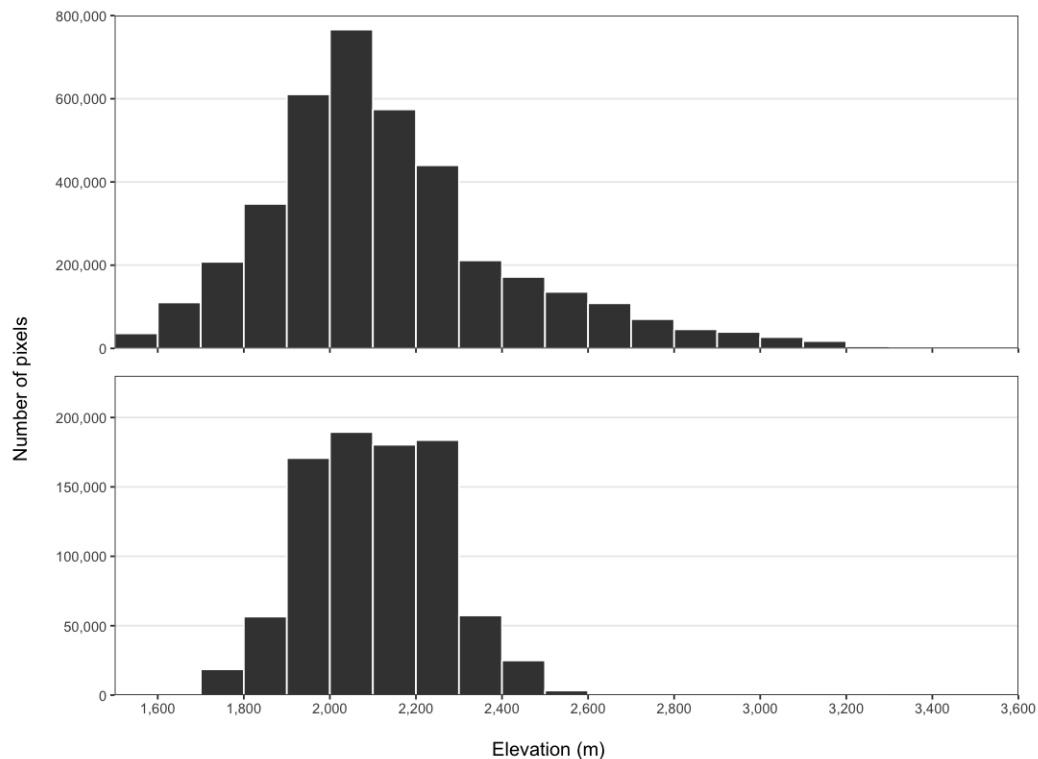
Figure 2.2. Frequency distributions of elevation within the entire extent of the Landsat P34/R35 scene (top panel) and the scene's piñon-juniper cover (bottom panel). Source: Shuttle Radar Topography Mission (SRTM) 90-m digital elevation dataset (Jarvis et al., 2008).
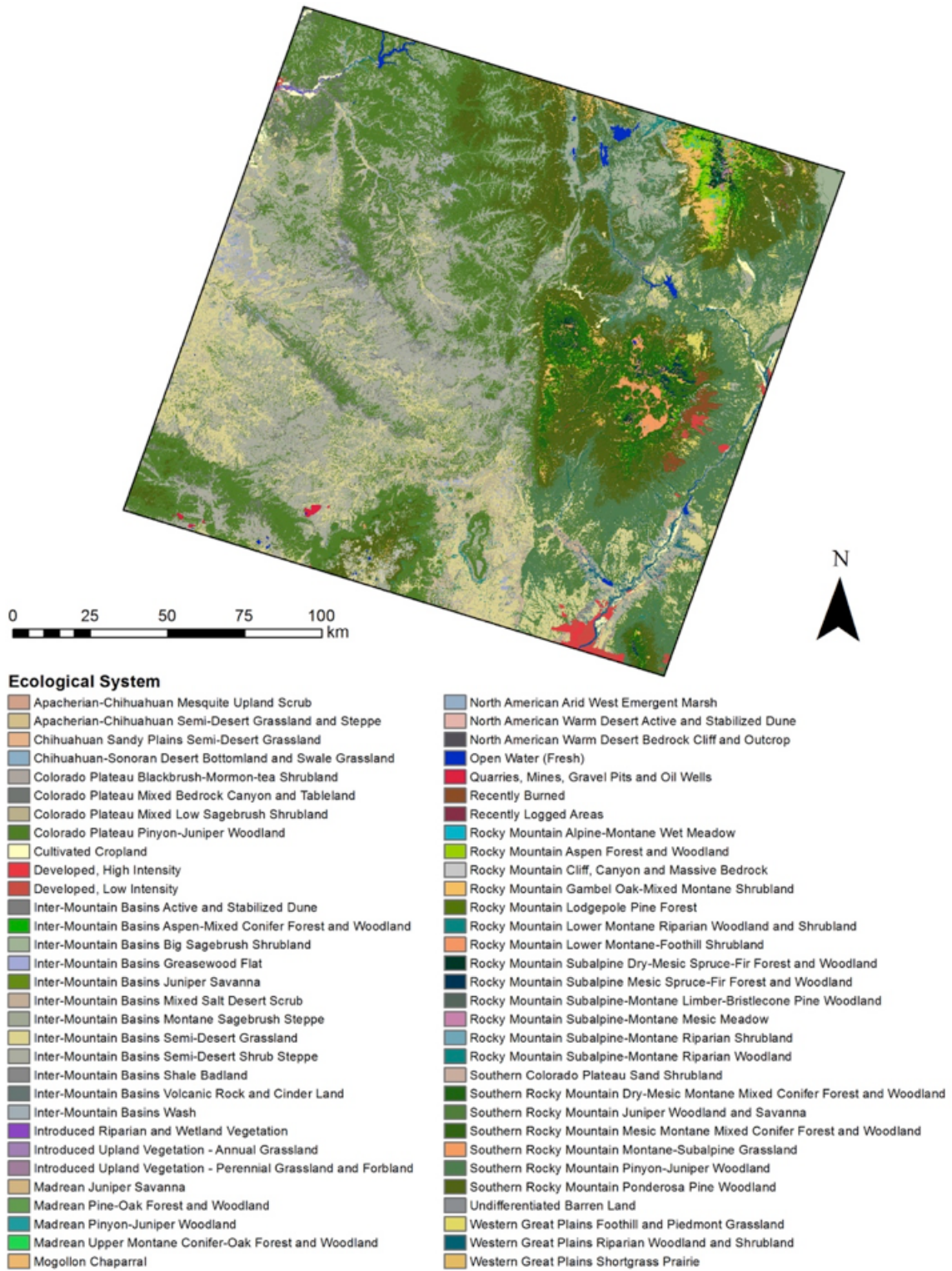
Figure 2.3. Ecological systems within the study area. Ecological systems are groups of plant community types that tend to co-occur within landscapes with similar ecological processes, substrates and/or environmental gradients (Comer et al., 2003). Source: National GAP land cover dataset (USGS, 2011).

The average annual precipitation in the area is 42.0 cm (1971-2000), with average annual maximum and minimum temperatures of 19.8 and 0.1 °C, respectively (Western Regional Climate Center, Bandelier N.M. station, 35.783 °N, 106.267 °W, elevation 1848 m; http://www.wrcc.dri.edu; accessed 19 May 2016). Elevation within the study area ranges from 1519 to 3515 m with a mean elevation of 2134 m, whereas the PJ woodlands within the study area have a mean elevation of 2105 m (Figure 2.2). There are 62 documented ecological systems within the study area (Figure 2.3; USGS, 2011). Of those 62, the Colorado Plateau Pinyon-Juniper Woodland is the most dominant ecological system documented (∼20% of total study area). These woodlands are the predominant low elevation woodlands of this region, occurring on warmer, dry mountain slopes, foothills, mesas, plateaus, and ridges (USGS, 2011). The two most common tree species found within the overstory of this ecological system are the two-needle piñon (*Pinus edulis*) and the Utah juniper (*Juniperus osteosperma*), with a variety of shrubs and grasses in the understory (USGS, 2011).

2.2. Landsat data preparation

This study utilized a 25-year time series (1987-2011) of Landsat Climate Data Record (CDR) images for Path 34, Row 35 (Table 2.1). Landsat CDRs are a high-level surface reflectance product that are derived from Level 1 terrain-corrected Landsat data and calibrated to surface reflectances using a digital elevation model (DEM) and the Landsat Ecosystem Disturbance Adaptive Processing System (LEDAPS; Masek et al., 2006). In addition, CDR scenes include associated quality assurance (QA) bands and an automatically generated cloud, cloud shadow, snow, and water mask (CFmask; Zhu and Woodcock, 2012). The scenes were obtained from the USGS EarthExplorer Archive (http://earthexplorer.usgs.gov). They were selected during the summer months (May-September) and with minimal cloud cover. Considerable cloud cover prevented the use of anniversary dates for images; however, sixteen of the twenty-five images were acquired

Table 2.1. Landsat Climate Data Record (CDR; USGS, 2016) imagery used in this study. All CDR scenes used were derived from the Landsat 5 Thematic Mapper sensor for Path 34, Row 35. Scene cloud cover is the percent of pixels in an image classified as cloud or cloud shadow. Piñon-juniper (PJ) cloud cover is the percent of pixels classified as cloud or cloud shadow within the distribution of PJ woodland within the scene. PJ distribution determined by the National GAP land cover dataset (USGS, 2011).

Year	Month/Day	Day of year	Scene cloud cover (%)	PJ cloud cover (%)
1987	June 22	173	0.01	0.01
1988	June 8	160	0.01	0.01
1989	July 5	186	0.02	0.01
1990	June 30	181	4.69	3.14
1991	June 17	168	0.56	0.39
1992	July 5	187	0.11	0.09
1993	June 22	173	0.02	0.01
1994	June 9	160	0.02	0.02
1995	June 12	163	0.25	0.20
1996	May 29	150	0.03	0.02
1997	July 3	184	0.02	0.02
1998	Aug. 7	219	3.69	2.82
1999	June 7	158	0.02	0.02
2000	Sept. 13	257	0.21	0.16
2001	June 12	163	16.09	11.67
2002	June 15	166	0.34	0.24
2003	July 4	185	0.83	0.60
2004	June 4	156	0.35	0.23
2005	June 7	158	0.23	0.16
2006	June 10	161	0.78	0.59
2007	June 29	180	0.99	0.71
2008	May 30	151	0.22	0.16
2009	Aug. 21	233	0.79	0.56
2010	June 5	156	0.16	0.11
2011	June 24	175	0.17	0.12

during the month of June. In addition, cloud cover during summer months prevented the use of images in years prior to 1987.

The preparation of this time series included several steps (Figure 2.4). First, I masked pixels containing clouds, cloud shadows, and water areas from each scene in the time series using the associated CFmask. Non-piñon-juniper vegetation and burned areas were masked by using geospatial land cover data from the National Gap Analysis Program (GAP; USGS, 2011) and the Monitoring Trends in Burn Severity Project (MTBS; Eidenshink et al., 2007), respectively. Second, for each image (year) in the time series, I calculated band ratios and spectral indices that have proven useful in past studies of climate-related tree mortality (e.g., Huang et al., 2010; Meigs et al., 2011; Garrity et al., 2013; Meddens et al., 2013; Meddens

DATA PREPARATION

0.6-m classification of piñon pine mortality between 2002 & 2006 (Garrity et al. 2013)

30-m Landsat CDR surface reflectances (1987-2011)

Mask non-PJ vegetation, clouds, and fire burn areas

Aggregate to 30-m pixels (Landsat resolution)

Calculate temporal anomalies from a per-pixel 1990-99 mean

Calculate spectral indices

30-m percent tree mortality (PTM) reference image

30-m Landsat-derived explanatory variables

OBJECTIVE 1

partition pixels for k-fold cross-validation

$k = 10$

$k = 7$

Build ZIB regression model

Build two-step RF model

Build single-step RF regression model (unbalanced)

Build single-step RF regression model (balanced)

Evaluate models

Optimal statistical model for predicting within-pixel PTM

OBJECTIVE 2

Apply model to entire Landsat time series (1987-2011)

Post-application correction

30-m PTM time series (1987-2009)

OBJECTIVE 3

Documented spatial and temporal patterns of tree mortality

Figure 2.4. Workflow diagram of the methods used in this study for data preparation and each of the three research objectives. Boxes with solid outlines indicate products and boxes with dashed outlines indicate tasks. CDR, Climate Data Records; PJ, piñon-juniper; ZIB, zero-inflated beta; and RF, random forest.

and Hicke, 2014; Hart and Veblen, 2015; Schwantes et al., 2016) (Table 2.2). Third, for each spectral band, ratio, and index stack, I calculated a multi-date spectral anomaly (hereafter referred to as a "temporal anomaly" and denoted with a $'$) with respect to the per-pixel, pre-disturbance mean of the stack. A temporal anomaly represents the difference between a pixel's value at a given point in time and its pre-disturbance mean (Meddens et al., 2013; Meddens and Hicke, 2014). Per-pixel temporal anomalies were calculated as follows:

$$SI'_{x,y,t} = SI_{x,y,t} - \frac{\sum_{t'=1}^{n} SI_{x,y,t'}}{n} \tag{2.1}$$

where SI' is the temporal anomaly of a given Landsat-derived spectral index (SI) at pixel location x, y in year t; the first term $(SI_{x,y,t})$ in the right-hand side of Equation 2.1 is the value of the spectral index for that pixel in the given year; and the second term in the right-hand side of Equation 2.1 is the multi-year pre-disturbance mean for that pixel for the

Table 2.2. Landsat-derived spectral ratios and indices used in this study as candidate explanatory variables for building a statistical model to predict percent tree mortality within 30-m grid cells. Bands (B) refer to Landsat TM band order and the corresponding portion of the electromagnetic spectrum.

Spectral index	Acronym	Formula	Reference	Application
Red-Green Index	RGI	B3/B2	Coops et al. (2006)	Identifying the ratio of green-red foliage
Moisture Stress Index	MSI	B5/B4	Rock et al. (1986)	Identifying water-related conifer forest damage
Normalized Difference Vegetation Index	NDVI	(B4 - B3)/(B4 + B3)	Tucker (1979)	Identifying amount of green biomass
Soil-Adjusted Vegetation Index	SAVI	(B4 - B3)/(B4 + B3 + 0.5)*(1 + 0.5)	Huete (1988)	Adjust NDVI to account for background soil noise
Normalized Difference Water Index	NDWI	(B4 - B5)/(B4 + B5)	Gao (1996)	Identifying canopy water content
Normalized Burn Ratio	NBR	(B4 - B7)/(B4 + B7)	Lutes et al. (2006)	Identifying fire-caused mortality severity
Tasseled Cap Brightness	TCB	0.2043*B1 + 0.4158*B2 + 0.5524*B3 + 0.5741*B4 + 0.3124*B5 + 0.2303*B7	Crist (1985)	Identifying surface brightness
Tasseled Cap Greenness	TCG	-0.1603*B1 - 0.2819*B2 - 0.4934*B3 + 0.7940*B4 - 0.0002*B5 - 0.1446*B7	Crist (1985)	Identifying vegetation greenness
Tasseled Cap Wetness	TCW	0.0315*B1 + 0.2021*B2 + 0.3102*B3 + 0.1594*B4 - 0.6806*B5 - 0.6109*B7	Crist (1985)	Identifying water content indicative of plant vigor
Disturbance Index	DI	TCB - (TCG + TCW)	Healey et al. (2005)	Identifying gray-stage mortality

n undisturbed years (t'). Here, the pre-disturbance mean was calculated from the temporal period 1990-1999 (i.e., $n = 10$).

Radiometric correction of satellite imagery is often a prerequisite for producing high-quality scientific time series and accounting for real changes on the Earth's surface as opposed to artifacts of data acquisition. Pons et al. (2014) compared the accuracy between a CDR and a non-CDR Landsat time series for the production of classified maps. The non-CDR data was radiometrically corrected using two different techniques: a traditional manual approach and a proposed automated one. Both techniques resulted in only slightly improved ($<4\%$) classification accuracy (Pons et al., 2014). Furthermore, Vuolo et al. (2015) demonstrated that CDR surface reflectances are nearly as accurate as raw Landsat scenes that have had site-specific, manual atmospheric correction and are thus a suitable off-the-shelf product for land cover change studies. Therefore, no further radiometric correction of the CDR imagery was performed in this study.

2.3. Reference data preparation

As the response variable for model development and evaluation, I used Garrity et al.'s (2013) classification of tree mortality during the 2002 to 2006 drought period, which was derived from QuickBird satellite imagery pan-sharpened to 0.6-m spatial resolution. The images were preprocessed and classified as described by Garrity et al. (2013). The mortality classification was conducted on a 46-km^2 area in Bandelier National Monument, within the spatial extent of Landsat Path 34, Row 35 (Figure 2.1). Classes include live and dead tree pixels. The overall classification accuracy was 97.9% (Garrity et al., 2013). I aggregated this classification to a 30-m spatial resolution to match the spatial resolution of the coarser Landsat imagery and to produce a continuous measure (i.e., percentage) of tree mortality per Landsat-resolution "superpixel" (Figure 2.5). Here, I define within-pixel percent tree mortality (PTM) as follows:

$$PTM_{x,y} = \frac{n_{dead,x,y}}{n_{all,x,y}} \times 100 \qquad (2.2)$$
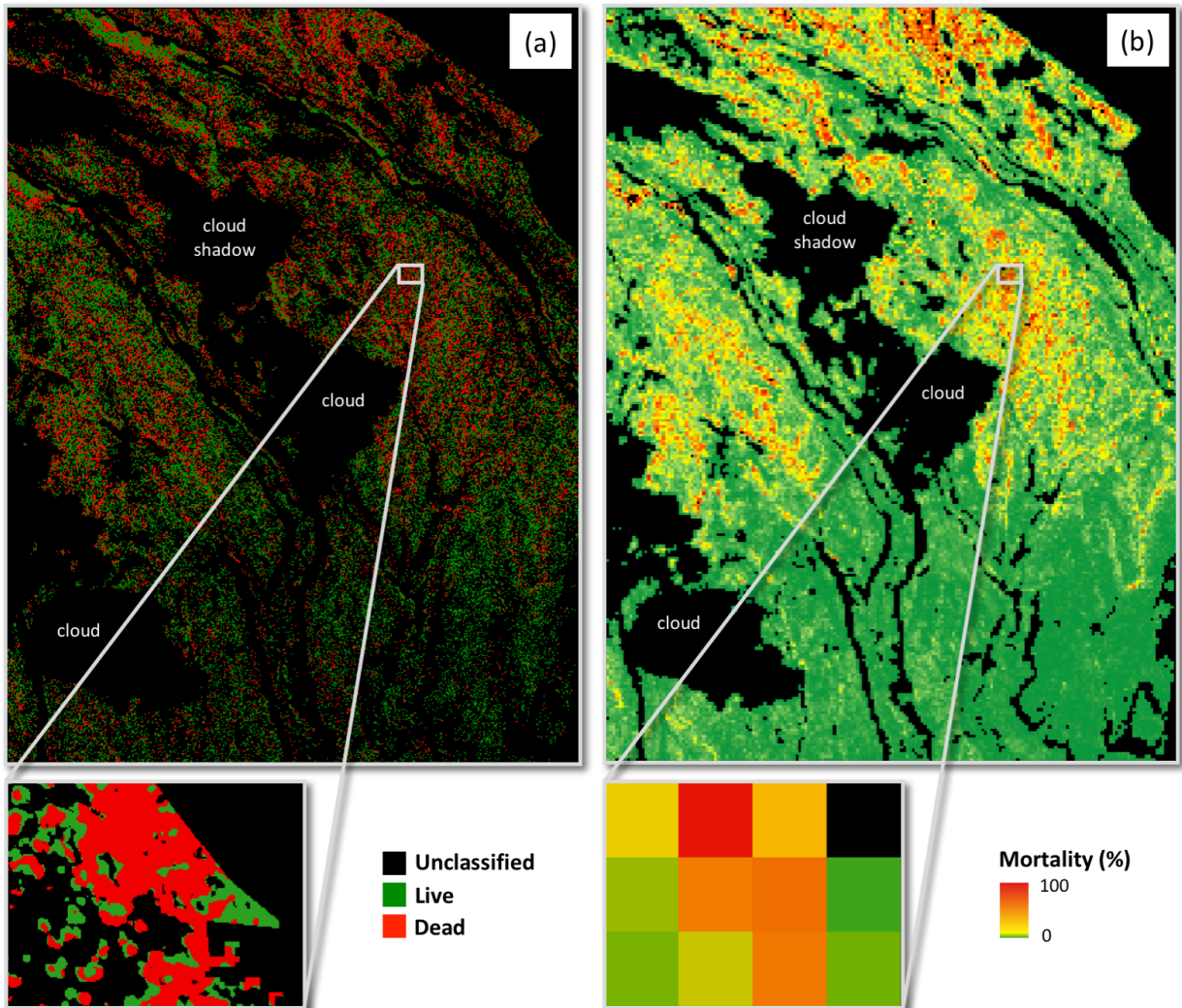
Figure 2.5. (a) Mortality classification (0.6 m), derived from 2002 and 2006 QuickBird imagery within Bandelier National Monument (Garrity et al., 2013). (b) Percent tree mortality (within 30-m grid cells), referred to as "reference data" within this study, calculated as the percent of 0.6-m pixels classified as dead within a Landsat-resolution (30-m) "superpixel".

where $PTM_{x,y}$ is the percent tree mortality at the (30-m) superpixel location x, y; n_{dead} is the number of 0.6-m pixels classified as dead within that x, y superpixel location; and n_{all} is the number of total (i.e., live, dead, and unclassified) 0.6-m pixels within that x, y superpixel location. Thus, for this study, PTM is defined as an absolute measure of mortality area within a superpixel, not relative to the total area of pre-disturbance tree canopy cover within a superpixel. The QuickBird-derived PTM image (Figure 2.5b) is hereafter referred to as "reference" data.

Investigating the distribution of PTM within the reference data revealed that only ~1% of the 30-m pixels contain greater than 50% within-pixel tree mortality (Figure 2.6). Meddens et al. (2013) showed that classification accuracy increases as percent mortality within a given 30-m grid cell increases. Conversely, classification accuracy decreases with decreasing percentages of within-pixel mortality for 30-m pixels. For example, Landsat pixels with <40% mortality, the classification accuracy reported was <50% (Meddens et al.,
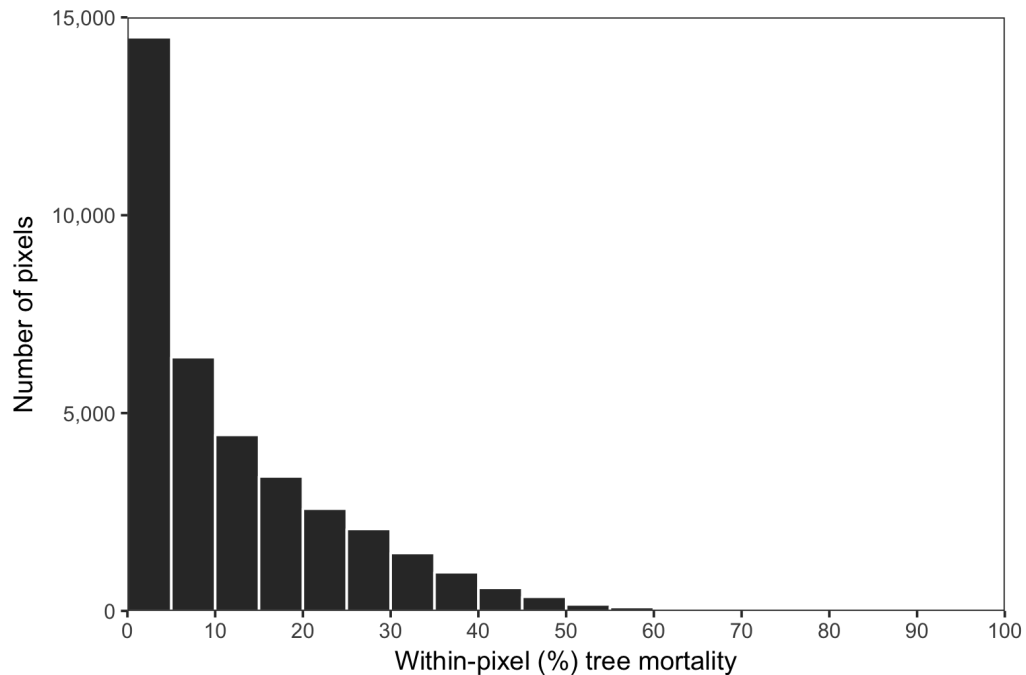
Figure 2.6. Distribution of percent tree mortality (PTM) within QuickBird-derived 30-m pixels used in this study as reference data for statistical model development and evaluation.

2013). Since here there are few pixels with high mortality in the reference data for model development and evaluation, a supervised classification of tree mortality would likely prove less accurate in predicting mortality. Thus, I chose to develop a statistical model to estimate severity (i.e., continuous proportions) of piñon mortality within a Landsat (30-m) time series, a method similar to past studies (Meddens and Hicke, 2014; Long and Lawrence, 2016; Schwantes et al., 2016). This approach offers a more sensitive representation of tree mortality within a given 30-m Landsat pixel compared to a binary (live/dead) classification.

2.4. Statistical modeling of percent tree mortality

I developed and evaluated statistical models for estimating continuous proportions of drought-induced tree mortality within a 30-m Landsat pixel, using zero-inflated beta (ZIB) regression and both single-step (regression) and two-step (classification–regression) random forest (RF) models (Table 2.3). As the response variable for all of the regression models, I used the aggregated reference data, which indicates within-pixel percent tree mortality (PTM). For the one classification model, the response variable was a binary presence/absence classification of mortality, where the percent tree mortality threshold for assigning absence or presence is further described in Section 2.4.2. For all of the statistical models, candidate explanatory variables consisted of individual Landsat TM bands, band

Table 2.3. Summary of zero-inflated beta (ZIB) regression and random forest (RF) models used in this study, including the corresponding balanced or unbalanced distribution of within-pixel percent tree mortality (PTM) used for model training and testing and the QuickBird-derived response variable. See Section 2.4.4. for a description of the unbalanced and balanced PTM distributions used.

Model framework	PTM distribution	Response variable
Single-step models		
ZIB regression	Unbalanced	PTM
RF regression	Unbalanced	PTM
RF regression	Balanced	PTM
Two-step model		
RF classification (step 1)	Unbalanced	P/A
RF regression (step 2)	Unbalanced	PTM

P/A, presence/absence of tree mortality within a 900m^2 pixel.

ratios (e.g., RGI, MSI), and vegetation indices such as Tasseled Cap brightness, greenness, and wetness (Table 2.2). In addition, the temporal anomalies from a 1990-99 pre-disturbance per-pixel mean of those spectral bands, ratios, and indices were used as candidate explanatory variables. In total, there were 32 Landsat-derived candidate explanatory variables considered for each year in the 25-year time series. I focused model development and evaluation on using the Landsat-derived explanatory variables from the year 2006 to match the spectral information of the reference image, which is a classification of PJ mortality between 2002 and 2006. All geoprocessing, statistical analyses, and data visualizations were performed using IDL (Exelis VIS, 2014), R (R Core Team, 2016), or ArcGIS (ESRI, 2015).

2.4.1. Zero-inflated beta regression modeling framework

ZIB regression uses a mixed continuous-discrete distribution: if the response variable is observed on the open interval (0, 1), then it is modeled with a continuous beta distribution through either linear or non-linear beta regression, and if the response is observed at the terminal point of zero, then it is modeled with a discrete component defined by a degenerate distribution at zero (Ospina and Ferrari, 2010, 2012). Here, the response variable of within-pixel (percent) tree mortality, y, was modeled with linear beta regression using the following probability density function under a ZIB distribution:

$$
bi(y; \alpha, \mu, \phi) = \begin{cases} \alpha, & \text{if } y = 0, \\ (1 - \alpha)f(y; \mu, \phi), & \text{if } y \epsilon (0, 1), \end{cases} \tag{2.3}
$$

where $f(y; \mu, \phi)$ is the density function for the beta distribution; α is the probability mass centered at zero (i.e., the probability of obtaining zero percent mortality in a 30-m grid cell); μ is the distribution mean if percent mortality is greater than zero; and ϕ is a precision parameter (also given that percent mortality is greater than zero) (Ospina and Ferrari, 2010, 2012). ZIB regression has been implemented in the R statistical software (R Core Team, 2016) package *GAMLSS* (Generalized Additive Model for Location, Scale and

Shape; Rigby and Stasinopoulos, 2005). Under the $GAMLSS$ package modeling framework, there are output predictions (i.e., predictive maps) for each of the distribution parameters (e.g., α, μ, ϕ). Using the outputs for α and μ, I assumed that if α, the probability of zero percent mortality, was >0.5, then the pixel had zero percent mortality; otherwise, the proportion of mortality within the pixel was predicted using μ, the distribution mean. Parameter estimation under $GAMLSS$ is performed by maximum likelihood (Rigby and Stasinopoulos, 2005). In consideration of the potential nonlinear relationships between the response and explanatory variables (e.g. Clifford et al., 2013), the $GAMLSS$ package allows for the parameters of the distribution of the response variable to be modeled as nonlinear parametric or nonparametric (i.e., smoothing) functions of the explanatory variables (Rigby and Stasinopoulos, 2005). We considered such relationships (Appendix A), but ultimately did not use them in the final ZIB regression model.

2.4.2. Random forest modeling framework

In addition to modeling percent tree mortality with ZIB regression, I also tested RF models. RF is a non-parametric machine learning algorithm that averages the predictions of multiple regression or classification decision trees (Breiman, 2001). Each decision tree in the ensemble is constructed using a different bootstrap sample of the input data and also a random subset of the predictor variables to chose the best split at each node in the tree (Breiman, 2001; Liaw and Wiener, 2002). Through this bootstrapping approach, RF is less sensitive to data skew (i.e., zero-inflation) and high dimensional data (in terms of over-fitting) than traditional parametric statistics (Breiman, 2001; Evans et al., 2011), making it a useful modeling approach for mapping percent tree mortality (e.g., Schwantes et al., 2016; Long and Lawrence, 2016). I tested two single-step RF regression models and one two-step RF (classification–regression) model. The first single-step model used RF in regression mode with training data as is (i.e., zero-inflated), whereas the second single-step model also used RF in regression mode, but used training data within the reference image that was sampled

across bins of percent mortality to create a balanced distribution. The two-step RF model first ran RF in classification mode to produce a binary classification of mortality presence or absence (Appendix B). To train this step of the model, the reference PTM response variable, y_i, was converted into a categorical presence/absence (P/A) variable, y_i^*, using the following thresholds:

$$y_i^* = \begin{cases} \text{absence} & \text{if } y_i \leq \theta, \\ \text{presence} & \text{if } y_i > \theta, \end{cases} \tag{2.4}$$

where several different PTM thresholds (θ) for assigning absence or presence were tested (i.e., $\theta = 0\%$, 5%, 10%, or 15%). The second step then runs RF in regression mode for pixels classified as having presence of mortality to estimate the proportion of that mortality within a 30-m grid cell. All RF models were run with 501 decision trees and a third of the total number of input explanatory variables were used to define each split. RF modeling was performed with the *ranger* package (Wright and Ziegler, 2015) for R (R Core Team, 2016).

2.4.3. Variable selection

Variable selection was performed to reduce the number of candidate explanatory variables, creating a more parsimonious model. Increasing parsimony has been seen to result in improved model fit and predictive performance with RF models (Evans et al., 2011). I initially sought to use a best subsets regression analysis to determine the optimal subset of explanatory variables, but was limited by computing power (32 total explanatory variables with over 23,000 observations in each variable). Thus I applied the variable selection methods used by Schwantes et al. (2016) for both ZIB regression and RF modeling. For variable selection with the ZIB regression model, two steps were involved, where (1) each explanatory variable was run in a separate bivariate ZIB regression model (i.e., one explanatory variable per model; 32 total models), and (2) a separate full model was run without that explanatory variable (i.e., 31 total explanatory variables per model; 32 total models). The first step allows one to infer variable importance while the second step allows one to infer variable

redundancy. For each of the 64 models, the generalized Akaike information criterion (GAIC) was calculated as:

$$GAIC = \hat{D} + d_\wp \tag{2.5}$$

where $\hat{D}$ is a measure of the lack of fit and the second term on the right-hand side of Equation 2.5 is a penalty for adding d parameters (Ospina and Ferrari, 2012). GAIC is recommended for use over AIC when there may be concern for model misspecification (e.g., incorrectly chosen link functions, neglected nonlinearities, omitted variables, etc.) or there is high skewness (i.e., Figure 2.6) within the data (Bozdogan, 2000; Ospina and Ferrari, 2012). Variables were then ranked by mean GAIC across the ten-times repeated model development and evaluation. Next, multicollinearity among the 32 candidate explanatory variables (Landsat TM Bands 1-5 and 7, spectral ratios/indices, and temporal anomalies) was assessed and redundant variable pairs ($|r| \geq 0.95$) were identified across all explanatory variable pairs for the year 2006 (e.g., Appendix C). For each redundant variable pair, one variable was removed by preferentially keeping variables with the lowest (i.e., most negative) mean GAIC value (Symonds and Moussalli, 2011; Schwantes et al., 2016) based on these two metrics (importance and redundancy). To create a more parsimonious model, the four most important and non-redundant variables were kept in the final ZIB regression model.

For variable selection with the RF models, a full model was built containing all 32 candidate explanatory variables (Table 2.4) using k-fold cross-validation (where $k = 10$ for the models with "unbalanced" training/testing data and $k = 7$ for the model with "balanced" training/testing data as further described in Section 2.4.4.). RF variable importance estimates were obtained for each fold and then averaged by variable. Again, for each redundant variable pair ($|r| > 0.95$), one variable was removed by preferentially keeping variables with the highest mean RF variable importance estimate across folds. Another model was then built using the remaining non-redundant variables to obtain new measures of variable importance. To create more parsimonious models, I kept only those variables

Table 2.4. Range of values for all Landsat-derived candidate explanatory variables in 2006 within the spatial extent of the reference image compared to the range of values within the study area.

| Variable | Reference image | | % of pixels in study area outside of range |
	Minimum value	Maximum value	
B1	0.0181	0.2224	0.08
B2	0.0236	0.2548	0.61
B3	0.0265	0.2723	3.13
B4	0.0364	0.3641	0.94
B5	0.0271	0.3893	25.37
B7	0.0181	0.3650	23.04
RGI	0.7029	1.4656	0.23
MSI	0.4115	2.2814	0.03
NDVI	-0.0228	0.7958	0.16
SAVI	-0.0132	0.5215	0.15
NDWI	-0.3905	0.4169	0.03
NBR	-0.4793	0.7099	0.01
TCB	0.0670	0.6987	5.79
TCG	-0.0242	0.2256	2.93
TCW	-0.3504	0.0145	22.66
DI	0.0712	0.9670	19.56
B1$'$	-0.0495	0.1379	0.09
B2$'$	-0.0777	0.1431	0.11
B3$'$	-0.1079	0.1541	0.07
B4$'$	-0.1892	0.1379	0.11
B5$'$	-0.2447	0.1551	0.21
B7$'$	-0.2294	0.1794	0.14
MSI$'$	-0.5545	1.2897	0.03
NDVI$'$	-0.3353	0.3039	0.15
SAVI$'$	-0.1801	0.2169	0.19
NDWI$'$	-0.4407	0.3249	0.10
RGI$'$	-4.7499	0.3261	0.07
NBR$'$	-0.6682	0.4050	0.03
TCB$'$	-0.3357	0.3082	0.07
TCG$'$	-0.0951	0.1044	0.21
TCW$'$	-0.1714	0.2269	0.17
DI$'$	-0.5340	0.4702	0.10

$'$ Temporal anomalies calculated from a 1990-99 per-pixel mean.

that were greater than the average measure of variable importance (e.g., Appendix D) in the final RF models.

2.4.4. Model development and evaluation

Two different approaches were used for model development and evaluation. For the first approach, I trained and tested models with all available reference data using stratified k-fold cross-validation, were $k = 10$. Because these data are zero-inflated, I refer to these

models as "unbalanced". Within each 10% mortality bin (i.e., 0-10%, 10-20%, etc.) the 30-m reference pixels and their corresponding explanatory variable pixels were partitioned into ten approximately equal-sized subsets for 10-fold cross-validation. Next, subsets of 10% of the data from each mortality bin were combined into ten separate data partitions. Thus, the reference data pixels were separated into ten approximately equal-sized data partitions with similar frequency distributions across bins of percent mortality (Appendix E). Models were then estimated ten times, each time (fold) using a different data partition for testing and the remaining nine partitions (one per PTM bin) combined for training. The 10-fold cross-validation approach was used with both ZIB regression, single-step RF regression, and two-step RF classification–regression models.

For the second approach, I developed models with training data balanced across bins of percent tree mortality to reduce the influence of the high-frequency low mortality pixels in model training and increase the influence of the low-frequency high mortality pixels (Haibo He and Garcia, 2009), hereafter referred to as the "balanced" model. For the balanced RF model, the total number of pixels that was sampled within each PTM bin was determined by the number of pixels available within the highest mortality bin within the reference image. Binning the reference data by increments of 10% (e.g., 0-10%, 10-20%, and so on), revealed that the highest mortality bin (70-80%) contained only eight pixels. However, by binning the data using increments of 15% (e.g., 0-15%, 15-30%, and so on), the highest mortality bin (60-75%) mortality contained 49 pixels. Therefore, the 15% mortality bins could be randomly sampled without replacement up to 49 pixels. Seven pixels from each 15% mortality bin were then combined into a data partition (fold), resulting in seven data partitions with balanced distributions across bins of percent mortality for model development and evaluation (Appendix F). This cross-validation approach was used with a single-step RF regression model.

To evaluate model performance for each of the final ZIB regression and RF models, predicted percent tree mortality was compared to the observed reference data across

ten- or seven-times repeated model building and evaluation, depending on which k-fold cross-validation approach was implemented. For regression models, several metrics of model performance were evaluated, including root mean square error (RMSE), mean absolute error (MAE), mean error (ME), and R^2. Although it is argued that MAE is the most unambiguous measure of average model performance error (Willmott and Matsuura, 2005), RMSE was considered more appropriate for model errors that followed a normal distribution (Chai and Draxler, 2014). RMSE, MAE, and ME were calculated as follows:

$$RMSE = \sqrt{\frac{1}{n}\sum_{i=1}^{n}(y_i - \hat{y}_i)^2} \tag{2.6}$$

$$MAE = \frac{1}{n}\sum_{i=1}^{n}|y_i - \hat{y}_i| \tag{2.7}$$

$$ME = \frac{1}{n}\sum_{i=1}^{n}(y_i - \hat{y}_i) \tag{2.8}$$

where n is the number of model errors; y_i is the ith percent tree mortality observation; and $\hat{y}_i$ is the ith percent tree mortality model prediction. For the two-step RF model, observations and predictions made during the first step (classification) were compared using a confusion matrix with two classes (presence/absence). Thus, individual class accuracies and overall classification accuracy metrics were obtained and averaged across ten-times repeated model development and evaluation.

Often with spatial data some degree of correlation is found between nearby observations in geographic space. The presence of spatial autocorrelation violates the assumption that observations in a set of measurements (e.g., a spectral index) are independent of each other. Two primary types of spatial autocorrelation exist, positive and negative. We used global Moran's I statistic to test for the presence of statistically significant ($\alpha = 0.05$) spatial autocorrelation within the residuals of the four different model

types (Moran, 1950). The null hypothesis of this test assumes spatial randomness (i.e., no spatial autocorrelation) whereas the alternative hypothesis is that there is presence of spatial dependence (autocorrelation). The global Moran's I statistic ranges from -1 to +1, whereby negative values indicate negative spatial autocorrelation and positive values indicate positive spatial autocorrelation. Final model selection was determined by two components: (1) the model performance metrics described in this section, and (2) the application of the model to the entire (spatial and temporal) extent of the Landsat time series, described in Section 2.5. Furthermore, I tested several other statistical modeling approaches, the results of which are reported in Appendix A.

2.5. Model application

Using only those pixels sampled within the region of the QuickBird-derived reference data, I determined the optimal statistical model through k-fold repeated model building and evaluation, as previously described in Section 2.4.. To apply a single final model to the entire Landsat time series (Objective 2), I generated a separate model using all available reference data and applied that model to the entire Landsat scene for each year in the 1987-2011 time series. The model predicted within-pixel percent tree mortality for only those pixels that were not masked during Landsat data preparation (described in Section 2.2.). Post-processing of the time series required several steps. First, I applied a percent tree mortality threshold value, below which predictions throughout the time series were reassigned to 0% mortality. This step was performed to account for uncertainty in model predictions associated with the combination of (a) potential background noise (soil, herbaceous cover, non-PJ woody cover, etc.) confounding the spectral signature of PJ mortality in a 30-m grid cell, (b) the possible influences of image-to-image radiometric variation across the Landsat time series, and (c) model overestimation at low mortality values, important because of the large amount of low mortality (Figure 2.6). To determine an appropriate threshold value, I tested the impact to the predicted mortality area time series of applying a series of different thresholds, from
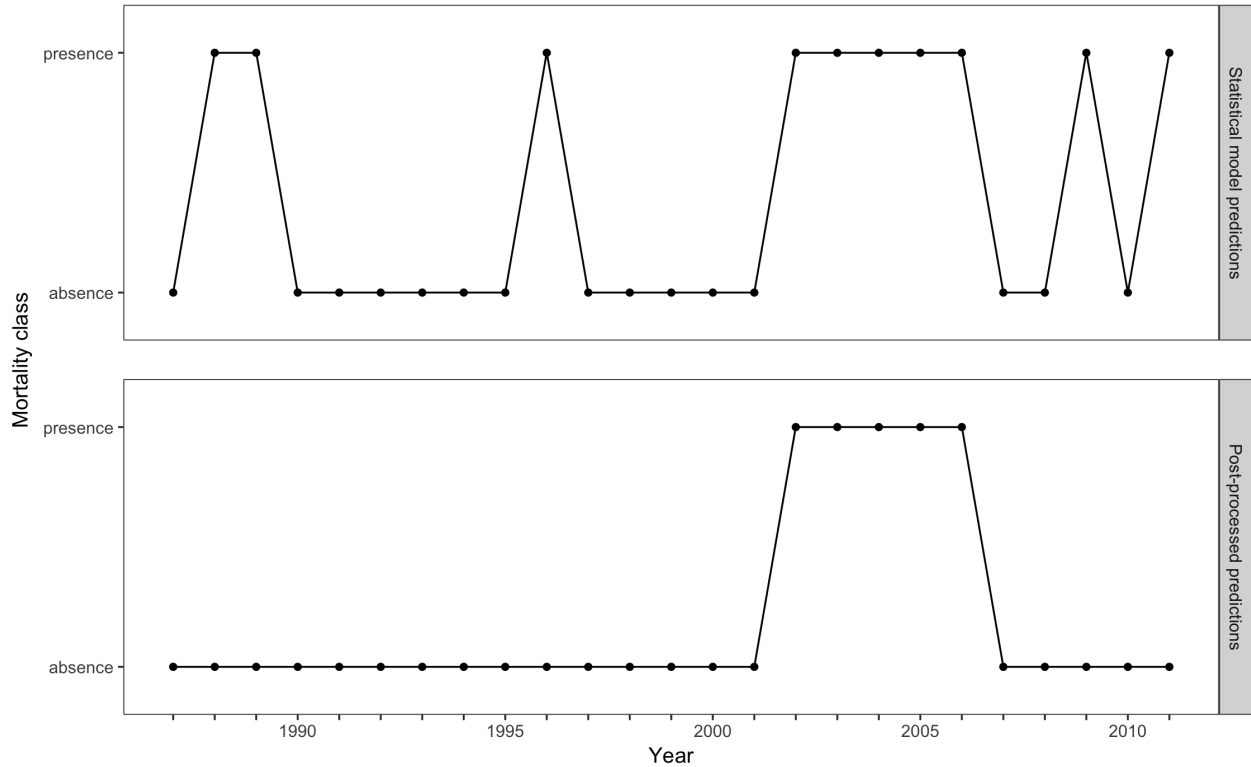
Figure 2.7. Example of the three-year (current and two subsequent years) moving-window approach for identifying mortality persistence (bottom panel) within a given pixel's predicted mortality presence/absence time series (top panel).

5% mortality to 30% in 5% increments. A threshold that decreased percent tree mortality predictions in years when no drought-induced tree mortality occurred was then selected. Once an appropriate threshold value was determined, pixels with percent tree mortality predictions below the threshold were set to zero and flagged as containing an absence of mortality. Pixels above the threshold were flagged as having presence of tree mortality.

Second, I masked non-temporally persistent predictions of mortality using a three year moving window on each pixel's binary (presence/absence) trajectory determined in the previous step (Figure 2.7). Beginning in the first year of the time series (1987), if a pixel was flagged as having presence of mortality, it was reassigned to absence (0% mortality) if it was not also flagged as presence in the subsequent two years; otherwise, the pixel was flagged as persistent mortality. Beginning in the second year of the time series (1988), if a pixel was flagged as presence of mortality, but it was not flagged as presence in the subsequent two

years, it was reassigned to absence only if the pixel had not also been flagged as persistent mortality in the previous year. Thus, by identifying persistence within the model-predicted percent tree mortality time series, false positive predictions were masked from the final time series. In addition, by applying a three year moving window (current and two subsequent years), the resulting tree mortality time series was limited temporally to the time period 1987-2009. Third, to ensure that predictions match the expected direction of disturbance (temporally), I computed cumulative percent tree mortality by requiring that percent tree mortality within a 30-m pixel only increase over time. Finally, annual percent tree mortality was calculated as the per-pixel difference in cumulative mortality between a given year and the subsequent year in the time series.

2.6. Assessing spatial and temporal patterns

Spatial and temporal patterns of the model-predicted tree mortality within the study area were assessed using several metrics. First, I measured duration of tree mortality, defined as the period from the start of tree mortality (i.e., $\geq 15\%$) to the first year with maximum cumulative mortality, calculated on a per-pixel basis and then averaged across the study area. Second, I measured the average rate of mortality, defined as the cumulative percent tree mortality in 2009 divided by the duration of tree mortality, again calculated on a per-pixel basis and then averaged across the study area. Third, I measured the average rate of mortality (units of percent tree mortality per year), assessed across both the entire distribution of piñon-juniper woodlands within the study area and only those pixels in which mortality presence was detected.

In addition, using the cumulative percent tree mortality time series (maps), I computed the total yearly and cumulative predicted mortality, in terms of area affected (hectares) and number of trees killed. Cumulative mortality area was calculated by summing cumulative percent tree mortality in 2009. To estimate the number of trees killed, I divided the area of tree mortality by the mean crown area of mature piñon pine trees (13.73 m^2;

95% confidence interval: 12.91-14.54 m^2, $n = 482$ trees), published by Meddens et al. (2012, Appendix A). I also assessed mortality patterns across subsets of elevation. I downloaded the Shuttle Radar Topography Mission (SRTM; Farr et al., 2007) DEM at the 30-m spatial resolution for the study area from the Google Earth Engine cloud-computing platform (Google Earth Engine Team, 2015).

Finally, I calculated the percent of PJ woodland area killed by drought. To do so, I needed to first calculate the total area (in hectares) of PJ woodlands within the study area. Because no accurate 30-m map of percent tree cover (PTC) for the PJ woodlands across our study area exists to date, I extrapolated the mean PTC of the reference data (31.82%) to the entire extent of the study area to estimate the total area of PJ cover within the study area. Therefore, the percent of PJ woodland area killed by drought estimated here assumes that the distribution of PTC within the reference data is representative of the distribution across the entire study area.

3. Results

3.1.   Comparison of statistical models

In general, variables comprised of temporal anomalies in 2006 from a per-pixel pre-drought (1990-99) mean, were the best predictors of percent tree mortality (Table 3.1). The only variable that was determined to be important across all of the final regression (ZIB and RF) models was NDVI$'$. Tasseled cap indices made up three out of the four final variables most important to the RF classification model for predicting presence/absence. NDWI$'$, TCW$'$, B5$'$, and NDVI$'$ was the variable combination that best predicted percent tree mortality using either the single-step RF regression model or the second step (regression) of the two-step RF model, both trained on pixels that were unbalanced across bins of percent tree mortality.

For the unbalanced two-step RF model, the overall classification accuracy for the first step (presence/absence) ranged from 76.2 to 96.71% across the different thresholds tested for assigning reference data pixels to presence/absence classes (Table 3.2). While the 0% threshold model resulted in the highest overall classification accuracy, the absence class omission error was 99.59% and the class commission error was 85%. Therefore, 10% was selected as the optimal threshold, because it resulted in the best balance between overall accuracy (76.2%) and class commission and omission errors. However, comparison between the 30-m reference observations and Landsat-derived predictions of percent tree mortality for the combined (classification–regression) two-step RF model resulted in an overall mean R^2 of 0.45 and an RMSE of 10.58%, the lowest and second highest, respectively, of the four model types (Table 3.1). Thus, the two-step RF model did not prove useful for predicting percent tree mortality and I do not report further results using this model.

For the unbalanced single-step RF model, comparison between the 30-m reference observations and Landsat-derived predictions of percent tree mortality resulted in an overall mean R^2 of 0.50 and an RMSE of 8.97% (Table 3.1). Comparably, the ZIB regression model

Table 3.1. Summary of model performance (predictions compared to observations) for the final single- and two-step random forest (RF) models and zero-inflated beta (ZIB) regression model. All metrics reported are averages over ten-times repeated model building and evaluation, except for the balanced single-step RF model, which are averages over seven-times repeated model building and evaluation. See Table 2.2 for explanatory variable acronyms.

Model	N	Selected explanatory variables[a]	R^2	RMSE (%)	MAE (%)	ME (%)	Moran's I[b] (p value)
ZIB regression	23055	MSI′ + TCG′ + TCW′ + NDVI′	0.52	8.64	6.365	-0.13	0.52 (<0.001)
RF regression (unbalanced)	22777	NDWI′ + TCW′ + B5′ + NDVI′	0.50	8.97	6.58	-0.12	0.51 (<0.001)
RF regression (balanced)	22777	DI′ + NBR′ + NDVI′ + SAVI′	0.45	13.71	10.17	-5.63	0.53 (<0.001)
Two-step RF combined	22777	–	0.45	10.58	7.93	1.60	0.37 (<0.001)
Step 1: classification	–	NBR′ + TCG′ + TCW′ + TCG	–	–	–	–	–
Step 2: regression	–	NDWI′ + TCW′ + B5′ + NDVI′	–	–	–	–	–

N, number of pixels used in cross-validation; RMSE, root mean square error; MAE, mean absolute error; ME, mean error.

[a] Ordered by variable importance, left (most) to right (least).

[b] Global Moran's I of the model residuals.

Table 3.2. Averaged confusion matrices for the first step (presence/absence classification) of the two-step random forest model. I tested different thresholds of percent tree mortality (0%, 5%, 10%, and 15%) for reassigning observations (less than or equal to) to zero. Class and total pixel values, overall classification accuracy, and confidence intervals reported are means of a cross-validation of ten classifications.

	Class	Reference Absence	Reference Presence	Total (pixels)	User's accuracy	Commission error
0% threshold						
Predicted	Absence	0.3	1.7	2.0	15.00%	85.00%
	Presence	73.2	2202.5	2275.7	96.78%	3.22%
	Total (pixels)	73.5	2204.2	2277.7		
	Producer's accuracy	0.41%	99.92%		Overall accuracy = 96.71%	
	Omission error	99.59%	0.08%		(CI[a] = 95.9–97.4%)	
5% threshold						
Predicted	Absence	497.1	208.2	705.3	70.48%	29.52%
	Presence	324.9	1247.5	1572.4	79.34%	20.66%
	Total (pixels)	822.0	1455.7	2277.7		
	Producer's accuracy	60.47%	85.70%		Overall accuracy = 76.60%	
	Omission error	39.53%	14.30%		(CI[a] = 74.83–78.29%)	
10% threshold						
Predicted	Absence	930.5	252.2	1182.7	78.68%	21.32%
	Presence	290.0	805.0	1095.0	73.52%	26.48%
	Total (pixels)	1220.5	1057.2	2277.7		
	Producer's accuracy	76.24%	76.14%		Overall accuracy = 76.20%	
	Omission error	23.76%	23.86%		(CI[a] = 74.46–77.86%)	
15% threshold						
Predicted	Absence	1275.3	249.5	1524.8	83.64%	16.36%
	Presence	228.6	524.3	752.9	69.64%	30.36%
	Total (pixels)	1503.9	773.8	2277.7		
	Producer's accuracy	84.80%	67.76%		Overall accuracy = 79.01%	
	Omission error	15.20%	32.24%		(CI[a] = 77.31–80.63%)	

[a] 95% confidence intervals averaged across the ten classifications.

resulted in an overall mean R^2 of 0.52 with an RMSE of 8.64%. The balanced single-step RF model resulted in an overall mean R^2 of 0.45, similar to the two-step RF model, and resulted in the highest mean RMSE (13.71%) of the four model types.

For each of the four types of models, I combined all predictions across the separate k-fold model evaluations to compare predicted PTM with the reference PTM data (Figure 3.1). These results reveal that RMSE was highest for the balanced single-step RF model and lowest for the ZIB regression model. Conversely, R^2 was highest for the ZIB
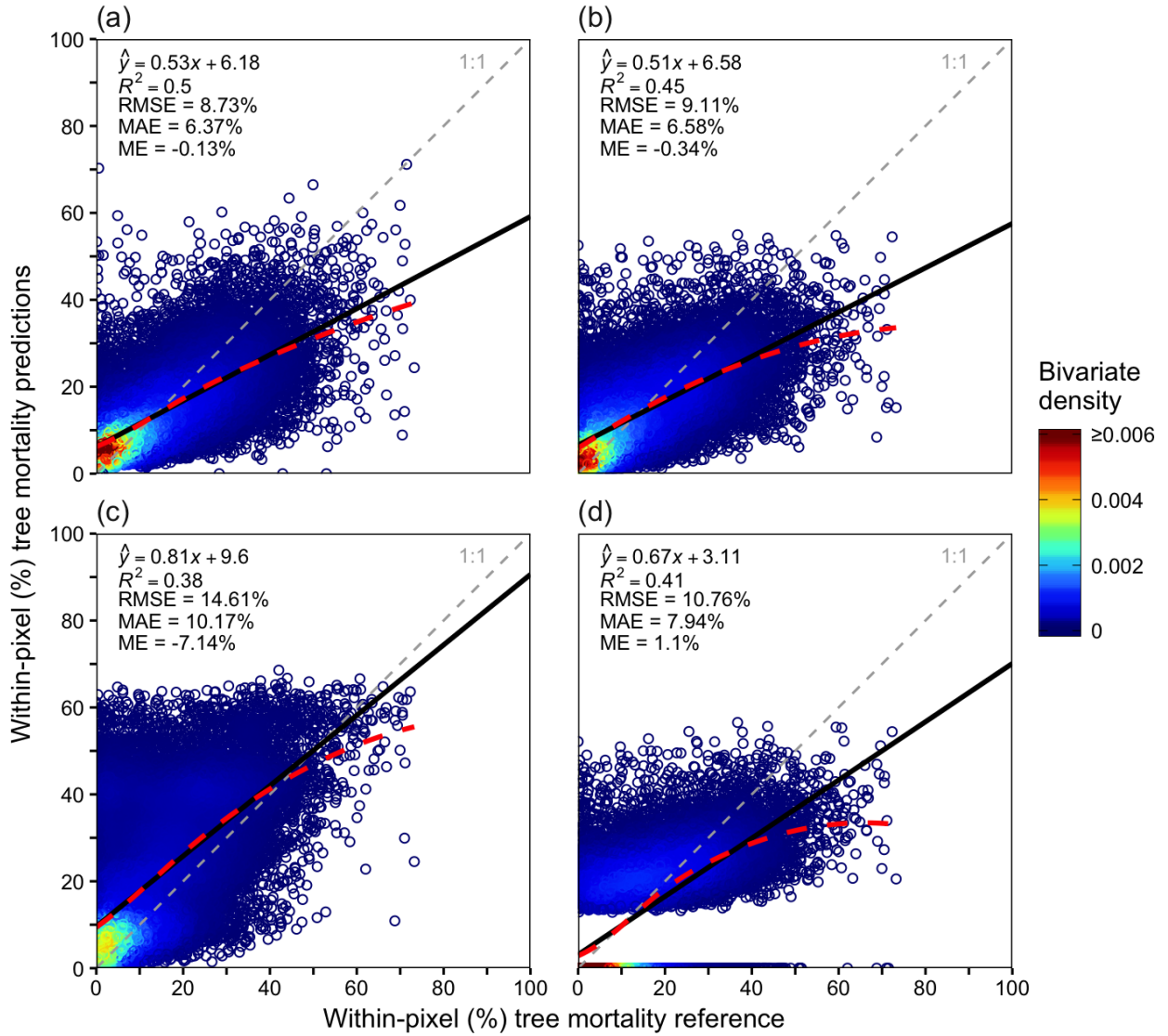
Figure 3.1. Comparison between reference data and predictions of the (a) ZIB regression model, (b) single-step unbalanced RF regression model, (c) single-step balanced RF regression model, and (d) two-step (classification–regression) RF model. Plots represent all predictions of k-fold model evaluation combined. Solid black lines indicate linear fit. Dashed red lines indicate Loess smoothed fits. Dashed gray lines are 1:1 lines. For (a), (b), and (d), the bivariate density of points was calculated using a bilinear weighted two-dimensional kernel density estimation.

regression model and lowest for the balanced single-step RF model. However, Figure 3.1 indicates that the single-step RF model resulted in the least amount of underestimation at higher levels of mortality severity. Furthermore, when the balanced RF model was evaluated using only those pixels sampled to create a balanced distribution across bins of PTM, RMSE ranged from 10.13 to 16.36% and R^2 ranged from 0.48 to 0.79 (Appendix G). In addition,
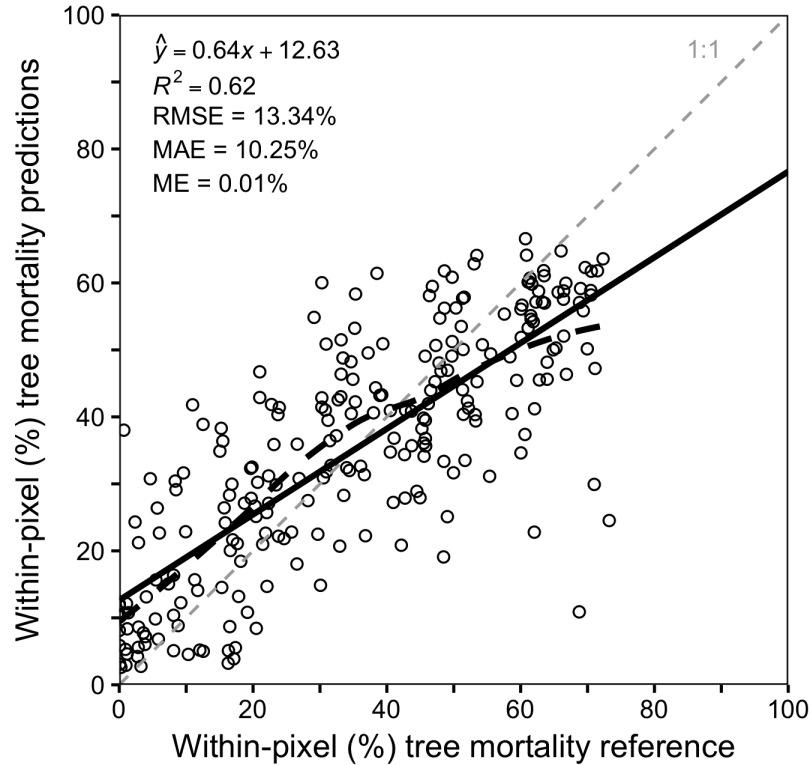
Figure 3.2. Comparison between reference and predicted PTM for the single-step random forest model with both training and testing data sampled to create a balanced distribution across 15% bins of tree mortality. Plot represents all predictions of seven-times model evaluation combined. Solid black line indicates linear fit. Dashed black line indicates Loess smoothed fit. Dashed gray line indicates the 1:1 line.

the frequency distributions of the explanatory variables for those reference pixels sampled for the balanced model are representative of the corresponding distributions across the entire reference image (Appendix H).

Statistically significant ($\alpha = 0.05$) positive spatial autocorrelation was found in the residuals of all model types (Global Moran's $I \geq 0.51$) evaluated using the entire reference image (Table 3.1). However, for the balanced single-step RF regression model, when evaluated using only the smaller sample of balanced pixels, no statistically significant spatial autocorrelation was found in the model residuals (Global Moran's $I = 0.027$, p-value $= 0.69$). In addition, when evaluated using only the balanced sample of data, the balanced RF model resulted in the highest R^2 (0.62) of any of the four model types (Figure 3.2). I selected the balanced single-step RF model as the optimal model for estimating percent tree mortality due to drought within this study.
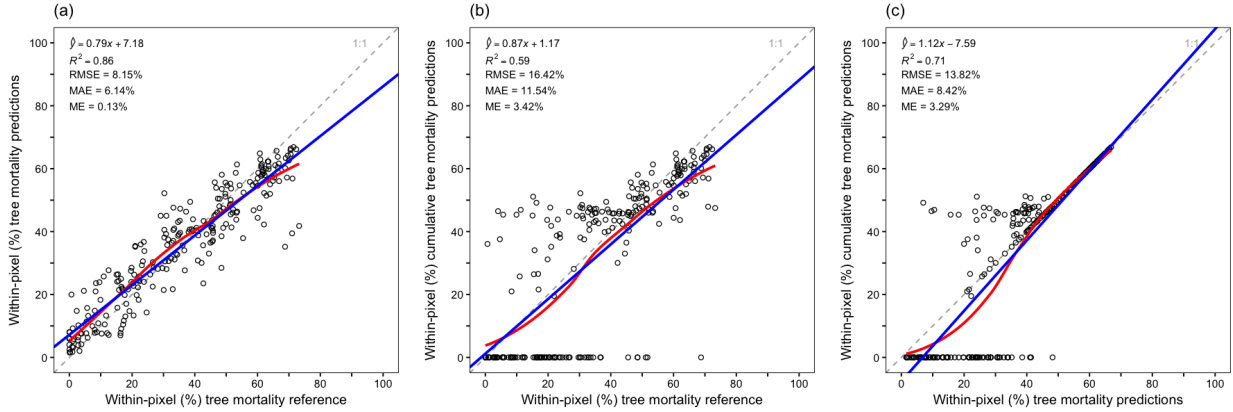
Figure 3.3. Comparisons between (a) reference PTM and the original single-step balanced RF model predictions of PTM, (b) reference PTM and the post-processed (cumulative) PTM predictions, and (c) the original single-step balanced RF model-predicted PTM and the post-processed (cumulative) PTM predictions. Solid blue lines indicate linear fit. Solid red lines indicate Loess smoothed fits. Dashed gray lines are 1:1 lines. Note, the single-step balanced RF model referenced here was developed using all available balanced training data and then used to predict PTM across the entire Landsat scene. Therefore, the model predictions (and the subsequent post-processed predictions) plotted here were not estimated through cross-validation and thus do not represent a set of independent test results; rather, (a) and (b) indicate goodness-of-fit between model predictions and the reference data used to train the model.

After model application to the entire Landsat scene (Objective 2), evaluation of goodness-of-fit between the balanced single-step RF model predictions (using all reference data) revealed strong agreement ($R^2 = 0.86$) and low prediction error (RMSE = 8.15%; Figure 3.3a). However, the post-processing technique implemented in this study (re-assigning low and non-temporally persistent predictions of percent tree mortality to zero) reduced the goodness-of-fit ($R^2 = 0.59$) and increased the prediction error (RMSE = 16.42%; Figure 3.3b). The decrease in model fit from the model-predicted percent tree mortality to the post-processed (cumulative) percent tree mortality predictions occurs below approximately 50% tree mortality (Figure 3.3c). The predicted values and the post-processed predictions showed good agreement ($R^2 = 0.71$) with a RMSE of 13.82% (Figure 3.3c).

3.2. Estimated tree mortality area

When evaluating thresholds to minimize model overestimation error, the 5% and a 10% tree mortality thresholds did not significantly reduce the overestimation of tree mortality

area in years prior to the early 2000s drought; however, the 15% mortality threshold did, in particular for 1996, both across the entire study area (Figure 3.4) and within the geographic extent of the reference data (Appendix I). Threshold values greater than 15% (i.e., 20-30%) reduced what we would expect to be overestimated tree mortality area in the years 1987-1990, 2000, and 2006, but did not eliminate the possible overestimation. Because we would not expect the model to predict drought-induced tree mortality in years prior to the early 2000s drought, I selected 15% as the optimal threshold for reducing model overestimation while retaining the widest range possible of model-predicted percent tree mortality (i.e., 15-68.5%). Thus, model predictions ≤15% tree mortality were reassigned to zero, with the most amount of pixels being re-assigned to zero in 2002 and 2006 (Appendix J). In addition, the post-processing persistence correction shortened the final tree mortality time series from 1987 to 2009 and reassigned tree mortality predications >15% to zero (Figure 3.3b).
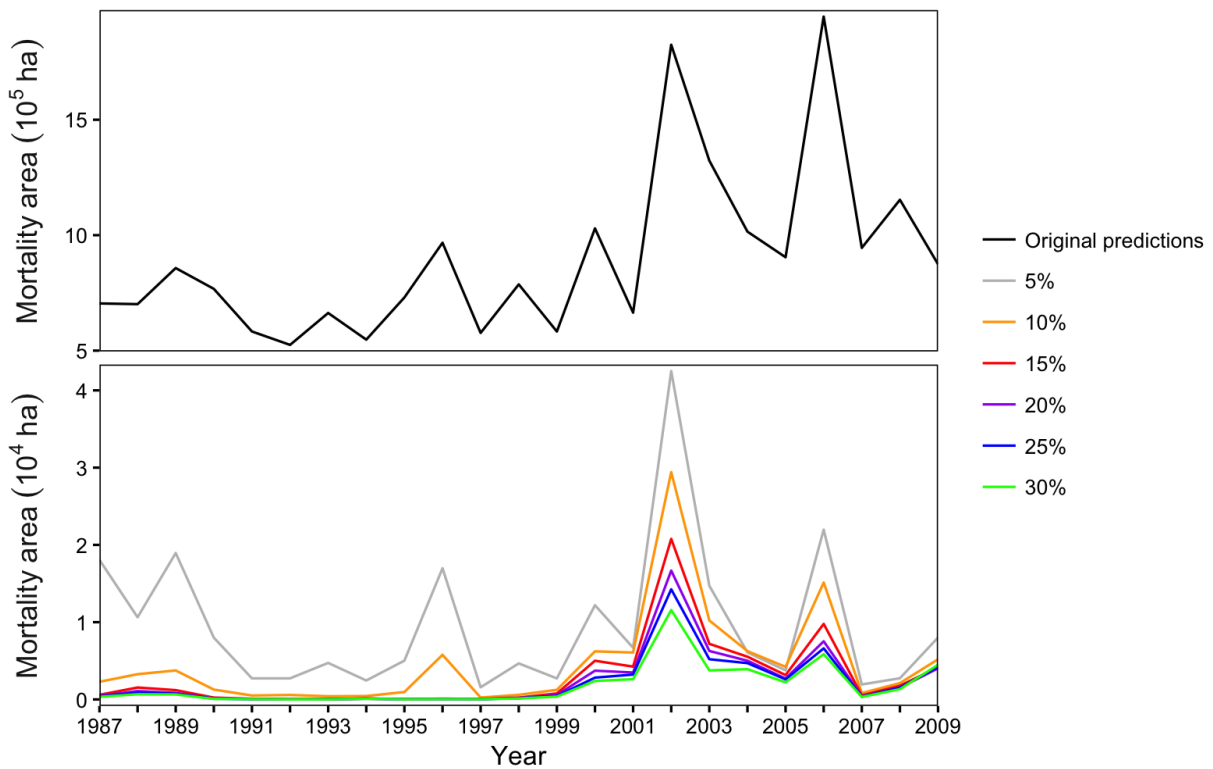
Figure 3.4. Time series of mortality area predictions from the final balanced single-step random forest model (top panel) and the post-processed mortality area time series using different thresholds (5%, 10%, ..., 30%) for reassigning low mortality severity predictions to 0% (bottom panel).
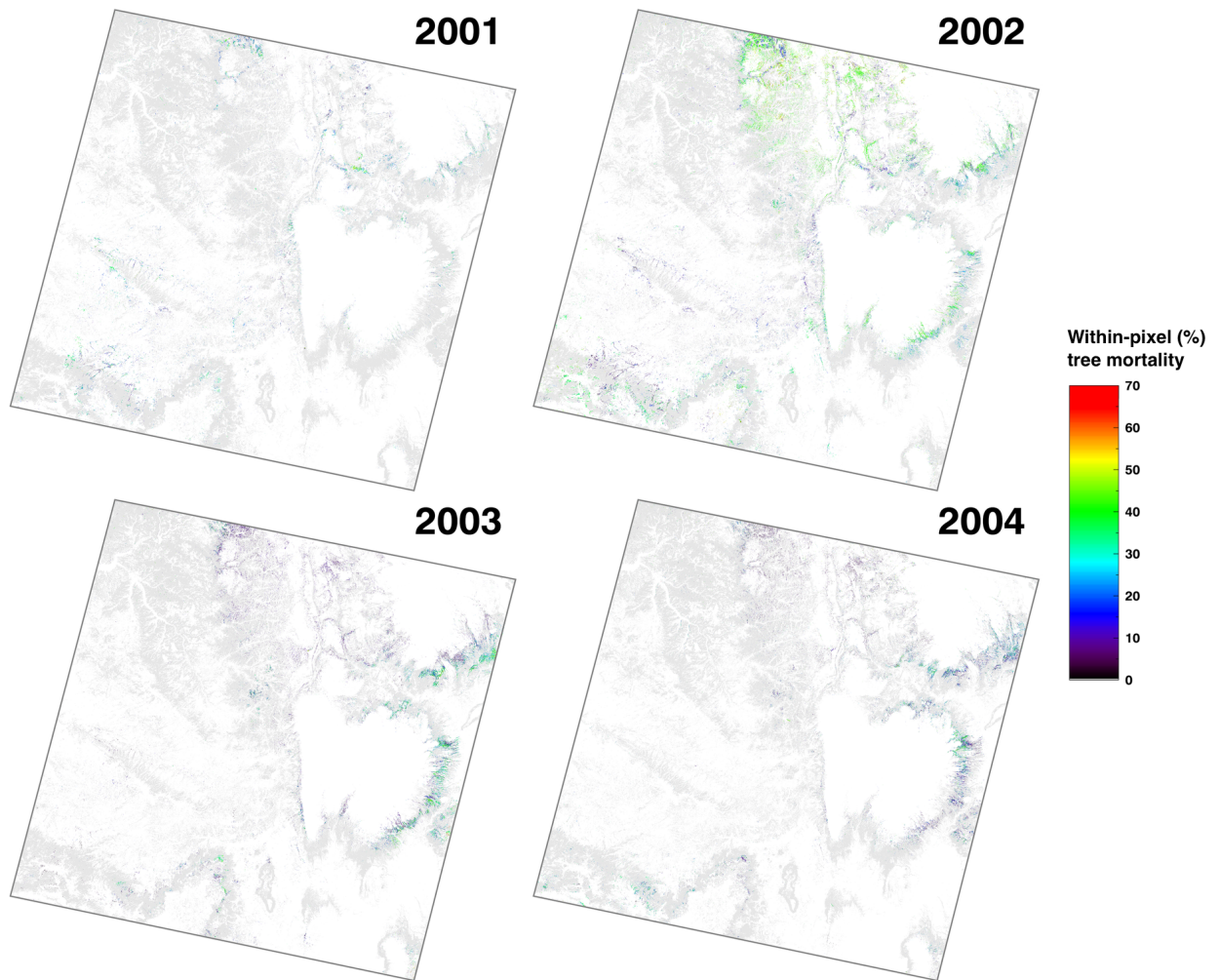
Figure 3.5. Within-pixel (percent) tree mortality across the study area for the time period 2001-2004 with a true color Landsat image from June 7, 1999. Note that year of satellite detection of tree mortality is shown. Gray pixels indicate areas within the piñon-juniper woodlands where no drought-induced tree mortality was detected.
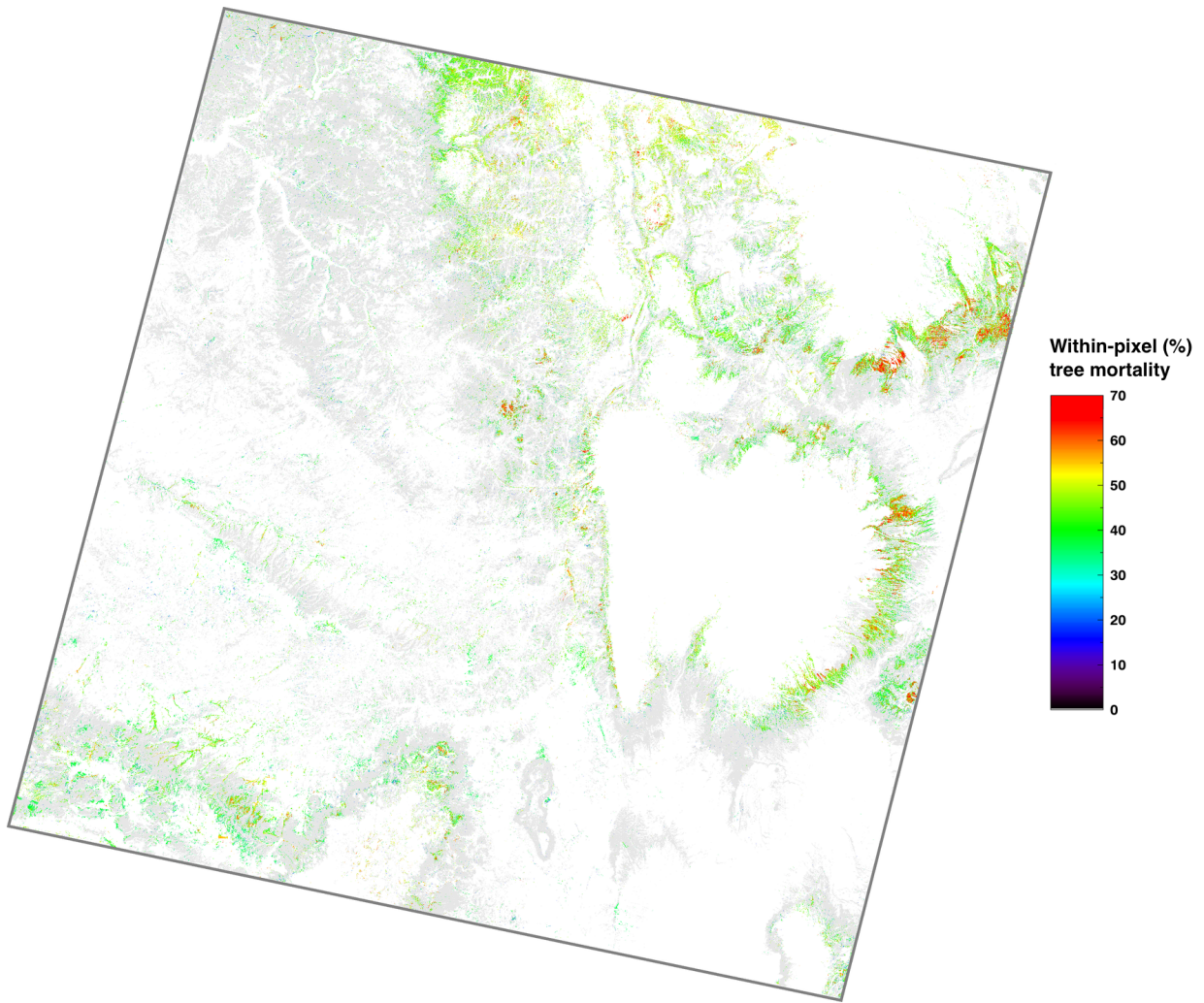
Table 3.3. Cumulative drought-induced tree mortality between 1987 and 2009 across different ranges of elevation. Area of tree mortality calculated by summing the product of cumulative percent tree mortality in 2009 and 30-m grid cells.

Elevation range (m)	Area of tree mortality (1,000 ha)	Number of killed trees[a] (millions)
< 1800	0.33	0.24 (0.23, 0.26)
1800–2000	7.05	5.14 (4.85, 5.46)
2000–2200	27.48	20.02 (18.89, 21.28)
2200–2400	27.44	19.99 (18.87, 21.25)
2400–2600	4.73	3.44 (3.25, 3.66)
≥ 2600	0.15	0.11 (0.10, 0.12)
All elevations	67.19	48.93 (46.19, 52.02)

[a] Area of tree mortality divided by the mean (and $\pm 95\%$ confidence interval) crown area of mature piñon pines trees (13.73 m^2; 95% confidence interval: 12.91-14.54 m^2, $n = 482$ trees), published by Meddens et al. (2012, Appendix A).

The first major impact to the Bandelier National Monument region within the time series occurred on the eastern side of the Jemez Mountains in 2002 (Figure 3.5). From 1987 to 2009, the northeast portion of the study area experienced the most cumulative percent tree mortality (Figure 3.6). Cumulative (in space and time) tree mortality in 2009 was 67,190 ha (Figure 3.7), or 19.8% of the piñon-juniper woodlands within the study area. 2002 experienced 20,773 ha of tree mortality, the most mortality area of any one year in the study period. Per-pixel cumulative percent tree mortality across the time series ranged from 15% to 68.5%, with an average of 42.3% and a standard deviation of 9.2%. The average per-pixel duration of mortality was approximately 3 years. The average per-pixel rate of tree mortality across the time series was 22% per year. However, including those pixels within the piñon-juniper woodlands for which zero percent tree mortality was predicted, the average rate of tree mortality decreased to 3.22% per year. Per-pixel maximum cumulative mortality was reached on average between 2004 and 2005. The predicted distribution of percent tree mortality within the study area (Figure 3.8) was more normally distributed for pixels >0% mortality compared to the reference data (Figure 2.6).

The lowest and highest elevation ranges experienced low tree mortality (0.33×10^3 ha and 0.15×10^3 ha, respectively; Table 3.3). The intermediate elevation ranges (2000-2200 m and 2200-2400 m) resulted in the highest predicted tree mortality (27.48×10^3 ha and 27.44×10^3 ha, respectively). Elevations of 1800-2000 m had 7.05×10^3 ha of tree mortality

Figure 3.6. Cumulative within-pixel (percent) tree mortality for the study area across the time period 1987-2009 with a true color Landsat image from June 7, 1999. Gray pixels indicate areas within the piñon-juniper woodlands where no drought-induced tree mortality was detected.

and 2400-2600 m resulted in 4.73×10^3 ha of mortality. The total estimated number of trees killed within the study area between 1987 to 2009 was 48.93 million piñon pines with a range of 46–52 million trees using a 95% confidence interval.
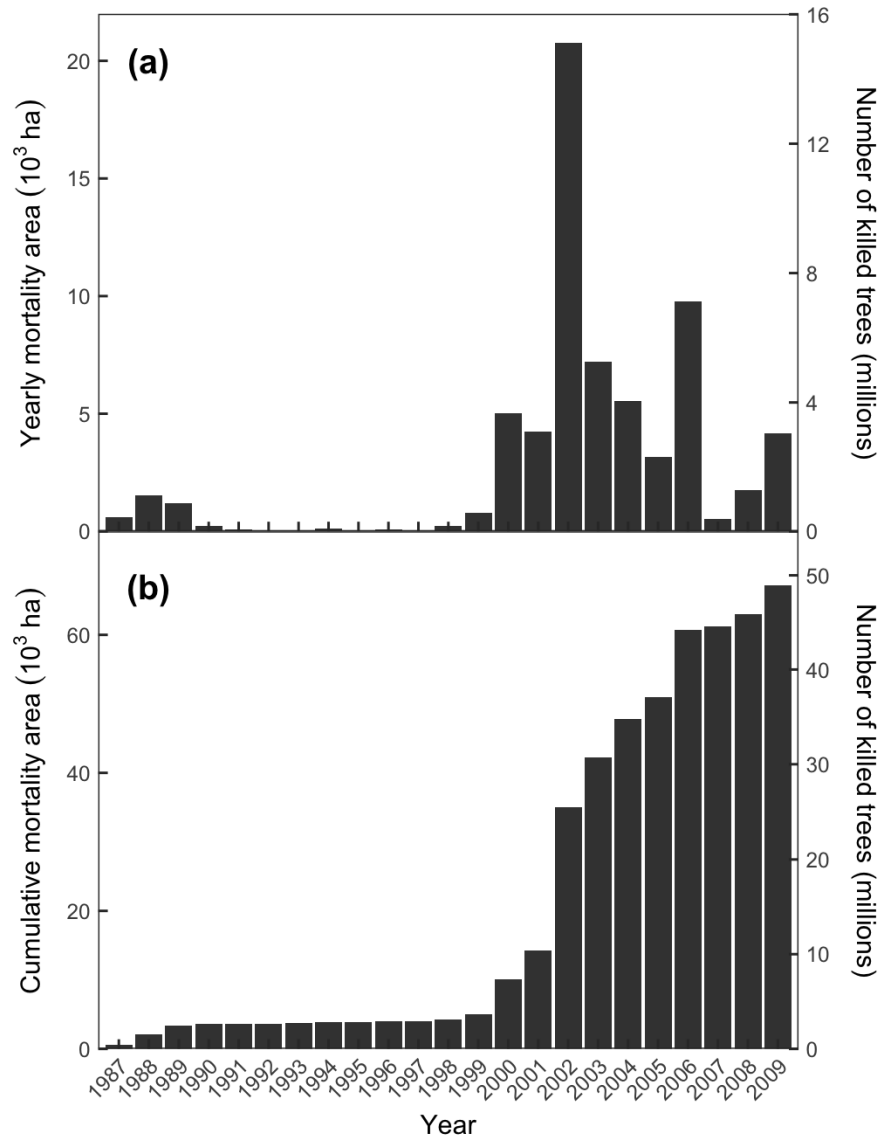
Figure 3.7. (a) Yearly and (b) cumulative drought-induced tree mortality (calculated by summing the product of percent mortality and 30-m grid cells) for the Landsat time series in total area (10^3 ha; left axis) and number of killed trees (right axes). Note that imagery in time series has varying amounts of cloud cover and fire burn areas. Year of detection of tree mortality is reported.
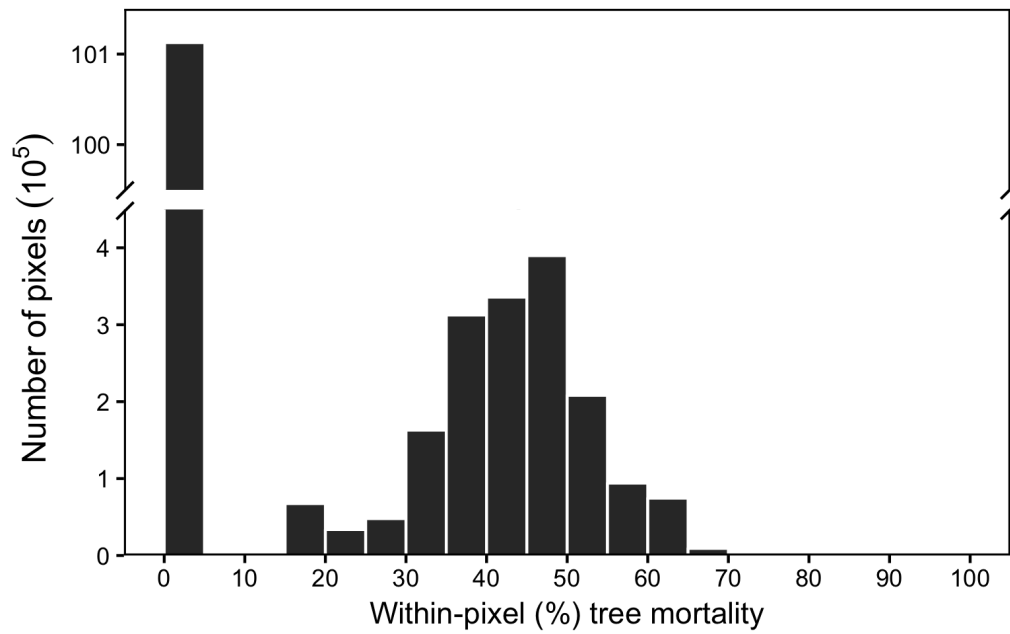
Figure 3.8. Frequency distribution of cumulative percent tree mortality predictions within the study area.

4. Discussion

The focus of this study was to produce a Landsat-based time series of percent tree mortality maps due to drought within the semi-arid open-canopy PJ woodlands and assess spatial and temporal patterns of that tree mortality. The results presented here corroborate the findings of several recent studies (e.g. Meddens and Hicke, 2014; Long and Lawrence, 2016; Schwantes et al., 2016) that it is possible to statistically model percent tree mortality over large areas (Figure 3.5), including drought-related mortality in semi-arid open-canopy woodlands (Schwantes et al., 2016), using a combination of moderate-resolution (e.g., Landsat) and finer-resolution (e.g., QuickBird) imagery. I evaluated two statistical modeling approaches suitable for modeling zero-inflated percent tree mortality data, ZIB regression and RF.

Based on model comparisons, I found ZIB regression resulted in lower error for predicting percent tree mortality compared with the RF approach (Table 3.1), similar to Schwantes et al. (2016). RF, however, resulted in the highest coefficient of determination among the four different types of models evaluated in this study (Figure 3.2). Schwantes et al. (2016) found the ZIB regression model to be less computationally demanding (i.e., ~20 times faster to run; ~5 times less memory required) than the RF approach. However, they used the *randomForest* R package (Liaw and Wiener, 2002) for RF modeling. In 2015 the R package *ranger* (Wright and Ziegler, 2015), was created for R to be a faster implementation of RF modeling for high dimensional data. Therefore, the *ranger* package was used in this study for RF modeling and I did not find a significant difference in speed or computational demand between the RF and ZIB regression models. Thus, computational differences did not influence final model selection in this study.

I tested two sampling designs (balanced and unbalanced) for model development and evaluation. I found that balancing the training and testing data sets across bins of percent tree mortality influenced model performance metrics. While the unbalanced single-step RF

model resulted in lower error compared with the balanced single-step RF model, balancing model training and testing data slightly increased the R^2. At low mortality, the unbalanced RF model resulted in reduced overestimation. Conversely, the balanced model resulted in reduced underestimation for higher percentages of tree mortality. Because of the zero-inflated nature of the data, the unbalanced RF model's lower error at low percent tree mortality resulted in lower RMSE than the balanced RF model. The improved representation of the balanced model across the range of percent tree mortality led to the higher R^2. I accounted for the overestimate of low percent tree mortality by the balanced model in post-processing. Furthermore, statistically significant positive spatial autocorrelation was found in the residuals of all models except for the balanced RF model. Thus, I suggest that the balanced model is more useful for predicting percent tree mortality compared to the unbalanced model in this situation. For these reasons, I used the balanced single-step RF model as the final model for predicting percent tree mortality.

Post-processing the time series of final model predictions was necessary to (a) reduce error related to relative radiometric variability among the Landsat CDR surface reflectances, (b) reduce false positives associated with predicting low percentages of tree mortality at the 30-m spatial resolution, and (c) account for model overestimation. Results revealed that a 15% mortality threshold nearly eliminated yearly mortality predictions in years where little to no drought-induced tree mortality occurred within the study area during the given time period. While results indicate that the post-processing steps developed here decreased goodness-of-fit between model predictions and reference data, they were useful in reducing error across the predicted tree mortality time series.

The spatial and temporal patterns identified here are similar to those of USDA Forest Service aerial detection surveys (ADS) (Meddens et al., 2012). For instance, both the maps produced in this study (Figure 3.5) and piñon pine mortality documented by both ADS data and Breshears et al. (2005) indicate that the most impacted regions within the study area are the eastern and northern sides of the Valles Caldera. In addition, studies of tree

mortality within the region (e.g. Breshears et al., 2005; Meddens et al., 2012) document that extensive drought-induced piñon pine mortality did not occur within these areas, particularly around the Jemez Mountains, until around 2002-2003, which is in line with the findings of this study. ADS data, in particular indicates that 2003 experienced more piñon mortality than 2002 within the study area, contrary to the results I report; however, the mortality event in 2002 was incompletely surveyed (Meddens et al., 2012) and likely experienced more widespread tree mortality than the following year (Breshears et al., 2005).

The 30-m tree mortality maps produced in this study are of a finer spatial resolution than those produced previously in the same region for the same time period by both Breshears et al. (2005) (1 km) and Meddens et al. (2012) (1 km), and in a similar open-canopy semi-arid woodland ecosystem by Schwantes et al. (2016) (60 m). In addition, Breshears et al. (2005) did not convert reported units of measurement from 2002-03 per-pixel NDVI deviations (relative to a pre-drought [1989-99] mean) to either percent tree mortality or mortality area. While Schwantes et al. (2016) used Landsat imagery, they aggregated pixels to the 60-m spatial resolution to minimize the introduction of misalignment errors between Landsat imagery and finer-resolution reference data. Here, I aggregated the finer-resolution reference data to align with and match the resolution of the Landsat imagery, resulting in percent tree mortality predictions at the 30-m spatial resolution as opposed to Schwantes et al.'s (2016) 60-m product.

Tree mortality was highest in 2002 and 2006. By the end of the study period (2009), cumulative tree mortality was widespread, affecting 19.8% of the PJ woodlands within the study area. The majority of pixels with PJ cover within the study area experienced <50% cumulative tree mortality and no pixel reached >70%. The most severely impacted areas were clustered in the intermediate elevation ranges within the northeast portion of the study area. The range of percent tree mortality is similar to other studies within the study area (e.g. Breshears et al., 2005; Clifford et al., 2008), whereas the average per-pixel rate (22% per year) and duration (3 years) of tree mortality within the study area are similar to other published

amounts within the beetle-affected lodgepole pine forests of nearby Colorado (Meddens and Hicke, 2014).

There are several caveats of this methodology for mapping percent tree mortality in open-canopy semi-arid woodlands with Landsat imagery. First, this approach does not separate tree, shrub, and plant species, resulting in a mixed-species overall prediction of percent tree mortality. The reported numbers of killed trees assume that all trees killed were piñon pines. Second, this approach does not separate drought-related disturbances. For example, direct drought-induced tree mortality from hydraulic failure and carbon starvation was not separated from drought-related insect outbreak. Beetle attack within the study area is thus interpreted as linked to drought. Also, I did not mask the Landsat time series for forest treatments or clearings within managed lands, which were likely minimal in the study area. However, I did control for fire-related mortality due to availability of spatially explicit fire burn area information (Eidenshink et al., 2007). Third, although the Bandelier National Monument region was one of the most severely impacted areas during the early 2000s drought, less than 1% of pixels within the reference data had >50% tree mortality, meaning that the statistical relationships established in model development did not include many observations of high severity mortality and may have been a source of bias in the final percent tree mortality predictions.

Mapping and assessing tree mortality is critical for understanding and monitoring its impacts to ecosystems and informing land managers. The maps and analyses presented here, however, can be used only as a baseline for assessing general spatial and temporal trends of tree mortality related to drought within the study area and period. These results increase understanding of the extent, timing, and severity of drought-induced tree mortality at the regional scale. The results of this study are not appropriate for forming spatiotemporally-explicit land management decisions without additional validation studies at the pixel-level.

Future research should consider several alternative directions that would likely improve the products of this study. The first is a spectral mixture analysis (SMA) or multiple endmember spectral mixture analysis (MESMA) approach. In open-canopy forests such as the semi-arid PJ woodlands, soils contribute more to the spectral reflectance within a given pixel, making changes in vegetation (i.e., mortality) a distinct challenge to detect with satellite imagery. SMA and MESMA are ways to overcome the spectral noise at moderate-to coarse-spatial resolutions (e.g., Huang et al., 2010). With SMA, a satellite image pixel can be decomposed via linear or nonlinear methods into multiple land cover components (e.g., woody biomass, herbaceous cover, bare soil, and urban development) expressed as proportions (i.e., percentages) of that pixel (Somers et al., 2011). SMA relies on collections (e.g., spectral libraries) of "pure" spectra (endmembers) that correspond to various land cover classes, collected either in the field or laboratory (Somers et al., 2011). Endmember selection, however, can be complicated by the inherent spatial and temporal variability within each of the various land cover classes as well as the scalability of "pure" spectra to the resolution of the observing sensor (Asner and Heidebrecht, 2002). Often endmembers can be obtained from "pure" pixels within the actual image, but this is challenging with moderate-resolution imagery in heterogeneous systems such as the semi-arid PJ woodlands. MESMA was developed to allow for within endmember variability (Roberts et al., 1998) and has recently been used in combination with Landsat imagery to separte drought-induced piñon and juniper mortality within the PJ woodlands of central New Mexico (Brewer et al., 2017).

Second, predictions of PTM would likely be improved by integrating topography (Schwantes et al., 2016) and spatial weighting (McCarley et al., 2017) into the statistical models developed here. Topographic variables (e.g., elevation, slope, and aspect) were not included as explanatory variables for model development in this study because future directions of this research include using the tree mortality maps produced here to identify environmental drivers of the mortality. Using topographic variables here to predict mortality

would then likely influence the statistical relationships yet-to-be-determined between the detected mortality and its drivers. It is recommended, however, that other studies consider including these variables as possible predictors in statistical models of tree mortality. In addition, simultaneous autoregressive modeling, a form of spatially weighted regression, can be used to better incorporate the presence of spatial autocorrelation found within the modeling results.

Finally, only one Landsat scene per year was used within this study. Future research should increase the number of scenes per year in the Landsat time series to reduce error associated with inter-seasonal variability. In addition, because it takes an average of nine months after mortality for piñon pines to drop their needles in semi-arid regions (Clifford et al., 2008), studies that use a Landsat time series with more than one scene per year will improve the understanding of the timing of landscape-scale PJ die-off.

5. Conclusions

I utilized Landsat imagery together with finer-resolution reference data to predict absolute percent tree mortality within a 30-m pixel, resulting in a representation of tree mortality more sensitive to patterns of severity, timing, and extent than a typical binary (live/dead) classification approach. In the semi-arid open-canopy ecosystem, post-processing model predictions were effective for reducing overestimation of mortality during years without drought. Drought-induced tree mortality within the study area lasted from around 2000 to 2009, with peaks in 2002 and 2006, resulting in 67,190 ha of cumulative tree mortality, or 19.8% of the PJ woodlands within the study area. On average, within-pixel tree mortality lasted 3 years, with 22% of a 30-m pixel experiencing tree mortality per year when mortality presence was detected. Within the study area, the lowest amount of tree mortality was found at both the lowest and highest elevation ranges, whereas the highest amount of tree mortality was found at the intermediate elevation ranges. I estimate that 48.9 million trees were killed within the study area between 1987 to 2009.

The satellite-based methods developed here and the results are useful to resource managers in the area (e.g., Bandelier National Monument) and scientists in the area (e.g., Los Alamos National Laboratory) studying tree mortality. The algorithms developed here to remotely monitor and map tree mortality with Landsat imagery contribute to the development of tree mortality mapping and monitoring efforts for open-canopy woodlands and forests. The maps created here provide a baseline for future research to quantify both drivers and impacts of this mortality. Furthermore, the spatial and temporal patterns documented here increase understanding of historical drought impacts to the piñon-juniper woodlands of northern New Mexico. By mapping tree mortality and documenting spatial and temporal patterns as this study has done, we can estimate ecological impacts and validate algorithms used in regional- or global-scale mortality models.

References

Allen, C. D. **2007**. Interactions across spatial scales among forest dieback, fire, and erosion in northern New Mexico landscapes. Ecosystems 10:797–808. http://dx.doi.org/10.1007/s10021-007-9057-4.

Allen, C. D., J. L. Betancourt, and T. W. Swetnam, **1998**. Chapter 9: Landscape Changes in the Southwestern United States: Techniques, Long-term Data Sets, and Trends. Technical report, U.S. Department of the Interior, U.S. Geological Survey. http://www.nbs.gov/luhna/southwest/southwest.html.

Allen, C. D., and D. D. Breshears. **1998**. Drought-induced shift of a forest–woodland ecotone: Rapid landscape response to climate variation. Proceedings of the National Academy of Sciences of the United States of America 95:14839–14842. http://www.pnas.org/content/95/25/14839.full.

Allen, C. D., D. D. Breshears, and N. G. McDowell. **2015**. On underestimation of global vulnerability to tree mortality and forest die-off from hotter drought in the Anthropocene. Ecosphere 6:1–55. http://dx.doi.org/10.1890/ES15-00203.1.

Allen, C. D., A. K. Macalady, H. Chenchouni, D. Bachelet, N. McDowell, M. Vennetier, T. Kitzberger, A. Rigling, D. D. Breshears, E. T. Hogg, P. Gonzalez, R. Fensham, Z. Zhang, J. Castro, N. Demidova, J.-H. Lim, G. Allard, S. W. Running, A. Semerci, and N. Cobb. **2010**. A global overview of drought and heat-induced tree mortality reveals emerging climate change risks for forests. Forest Ecology and Management 259:660–684. http://linkinghub.elsevier.com/retrieve/pii/S037811270900615X.

Anderegg, W. R. L., J. A. Hicke, R. A. Fisher, C. D. Allen, J. Aukema, B. Bentz, S. Hood, J. W. Lichstein, A. K. Macalady, N. McDowell, Y. Pan, K. Raffa, A. Sala, J. D. Shaw, N. L. Stephenson, C. Tague, and M. Zeppel. **2015**. Tree mortality from drought, insects, and their interactions in a changing climate. New Phytologist 208:674–683. http://doi.wiley.com/10.1111/nph.13477.

Anderegg, W. R. L., J. M. Kane, and L. D. L. Anderegg. **2012**. Consequences of widespread tree mortality triggered by drought and temperature stress. Nature Climate Change 3:30–36. http://dx.doi.org/10.1038/nclimate1635.

Asner, G. P., and K. B. Heidebrecht. **2002**. Spectral unmixing of vegetation, soil and dry carbon cover in arid regions: Comparing multispectral and hyperspectral observations. International Journal of Remote Sensing 23:3939–3958. http://www.tandfonline.com/doi/abs/10.1080/01431160110115960.

Bentz, B. J., J. Régnière, C. J. Fettig, E. M. Hansen, J. L. Hayes, J. A. Hicke, R. G. Kelsey, J. F. Negrón, and S. J. Seybold. **2010**. Climate Change and Bark Beetles

of the Western United States and Canada: Direct and Indirect Effects. BioScience 60:602–613. http://www.jstor.org/stable/10.1525/bio.2010.60.8.6.

Bozdogan, H. **2000**. Akaike's Information Criterion and Recent Developments in Information Complexity. Journal of Mathematical Psychology 44:62–91. http://www.ncbi.nlm.nih.gov/pubmed/10733858.

Breiman, L. **2001**. Random Forests. Machine Learning 45:5–32. http://link.springer.com/10.1023/A:1010933404324.

Breshears, D. D., N. S. Cobb, P. M. Rich, K. P. Price, C. D. Allen, R. G. Balice, W. H. Romme, J. H. Kastens, M. L. Floyd, J. Belnap, J. J. Anderson, O. B. Myers, and C. W. Meyer. **2005**. Regional vegetation die-off in response to global-change-type drought. Proceedings of the National Academy of Sciences of the United States of America 102:15144–15148. http://www.pnas.org/content/102/42/15144.abstract.

Breshears, D. D., L. López-Hoffman, and L. J. Graumlich. **2011**. When Ecosystem Services Crash: Preparing for Big, Fast, Patchy Climate Change. AMBIO: A Journal of the Human Environment 40:256–263. http://www.bioone.org/doi/abs/10.1007/s13280-010-0106-4.

Breshears, D. D., O. B. Myers, C. W. Meyer, F. J. Barnes, C. B. Zou, C. D. Allen, N. G. McDowell, and W. T. Pockman. **2009**. Tree die-off in response to global change-type drought: mortality insights from a decade of plant water potential measurements. Frontiers in Ecology and the Environment 7:185–189. http://doi.wiley.com/10.1890/080016.

Brewer, W. L., C. L. Lippitt, C. D. Lippitt, and M. E. Litvak. **2017**. Assessing drought-induced change in a piñon-juniper woodland with Landsat: a multiple endmember spectral mixture analysis approach. International Journal of Remote Sensing 38:4156–4176. http://dx.doi.org/10.1080/01431161.2017.1317940.

Bright, B. C., J. A. Hicke, and A. T. Hudak. **2012**. Estimating aboveground carbon stocks of a forest affected by mountain pine beetle in Idaho using lidar and multispectral imagery. Remote Sensing of Environment 124:270–281. http://dx.doi.org/10.1016/j.rse.2012.05.016.

Chai, T., and R. R. Draxler. **2014**. Root mean square error (RMSE) or mean absolute error (MAE)? – Arguments against avoiding RMSE in the literature. Geoscientific Model Development 7:1247–1250. http://www.geosci-model-dev.net/7/1247/2014/.

Clifford, M., M. Rocca, R. Delph, P. Ford, and N. Cobb. **2008**. Drought induced tree mortality and ensuing bark beetle outbreaks in Southwestern pinyon-juniper woodlands. Ecology, management, and restoration of pinon-juniper and ponderosa

pine ecosystems: combined proceedings of the 2005 St. George, Utah and 2006 Albuquerue, New Mexico workshops pages 39–51.

Clifford, M. J., P. D. Royer, N. S. Cobb, D. D. Breshears, and P. L. Ford. **2013**. Precipitation thresholds and drought-induced tree die-off: Insights from patterns of *Pinus edulis* mortality along an environmental stress gradient. New Phytologist 200:413–421. http://dx.doi.org/10.1111/nph.12362.

Comer, P. J., D. Faber-Langendoen, R. Evans, S. Gawler, C. Josse, G. Kittel, S. Menard, S. Pyne, M. Reid, K. Schulz, K. Snowand, and J. Teague. **2003**. Ecological systems of the United States: A working classification of US terrestrial systems. NatureServe, Arlington, Virginia.

Coops, N. C., M. Johnson, M. A. Wulder, and J. C. White. **2006**. Assessment of QuickBird high spatial resolution imagery to detect red attack damage due to mountain pine beetle infestation. Remote Sensing of Environment 103:67–80. http://www.sciencedirect.com/science/article/pii/S0034425706001283.

Coulston, J. W., G. G. Moisen, B. T. Wilson, M. V. Finco, W. B. Cohen, and C. K. Brewer. **2012**. Modeling Percent Tree Canopy Cover: A Pilot Study. Photogrammetric Engineering & Remote Sensing 78:715–727. http://www.treesearch.fs.fed.us/pubs/40860.

Crist, E. P. **1985**. A TM Tasseled Cap equivalent transformation for reflectance factor data. Remote Sensing of Environment 17:301–306. http://linkinghub.elsevier.com/retrieve/pii/0034425785901026.

Dale, V. H., L. A. Joyce, S. McNulty, R. P. Neilson, M. P. Ayres, M. D. Flannigan, P. J. Hanson, L. C. Irland, A. E. Lugo, C. J. Peterson, et al. **2001**. Climate change and forest disturbances: climate change can affect forests by altering the frequency, intensity, duration, and timing of fire, drought, introduced species, insect and pathogen outbreaks, hurricanes, windstorms, ice storms, or landslides. BioScience 51:723–734. http://www.bioone.org/doi/full/10.1641/0006-3568%282001%29051%5B0723%3ACCAFD%5D2.0.CO%3B2.

Dick-Peddie, W. A. **1993**. New Mexico vegetation: past, present, and future. University of New Mexico Press, Albuquerque, New Mexico.

Eidenshink, J., B. Schwind, K. Brewer, Z.-l. Zhu, B. Quayle, and S. Howard. **2007**. A Project for Monitoring Trends in Burn Severity. Fire Ecology 3:3–21.

Eskelson, B. N., L. Madsen, J. C. Hagar, and H. Temesgen. **2011**. Estimating riparian understory vegetation cover with beta regression and copula models. Forest Science 57:212–221. http://www.ingentaconnect.com/content/saf/fs/2011/00000057/00000003/art00005.

ESRI, **2015**. ArcGIS, versions 10.3-10.4. Environmental Systems Research Institute, Redlands, California. http://www.esri.com/.

Evans, J. S., M. A. Murphy, Z. A. Holden, and S. A. Cushman, **2011**. Modeling Species Distribution and Change Using Random Forest. Pages 139–159 *in* Predictive Species and Habitat Modeling in Landscape Ecology. July 2017, Springer New York, New York, NY. http://link.springer.com/10.1007/978-1-4419-7390-0_8.

Exelis VIS, **2014**. Interactive Data Language, version 8.4. Exelis Visual Information Solutions, Boulder, Colorado. http://www.exelisvis.com/.

Farr, T. G., P. A. Rosen, E. Caro, R. Crippen, R. Duren, S. Hensley, M. Kobrick, M. Paller, E. Rodriguez, L. Roth, D. Seal, S. Shaffer, J. Shimada, J. Umland, M. Werner, M. Oskin, D. Burbank, and D. Alsdorf. **2007**. The Shuttle Radar Topography Mission. Reviews of Geophysics 45. http://dx.doi.org/10.1029/2005RG000183.

Ferguson, C. A., **2006**. Detection of pinyon mortality in northern New Mexico using remotely sensed data and linear methods. Master's thesis, University of New Mexico. Department of Geography. Unpublished thesis.

Ferrari, S., and F. Cribari-Neto. **2004**. Beta Regression for Modelling Rates and Proportions. Journal of Applied Statistics 31:799–815. http://www.tandfonline.com/doi/abs/10.1080/0266476042000214501.

Gao, B. **1996**. NDWI–A normalized difference water index for remote sensing of vegetation liquid water from space. Remote Sensing of Environment 58:257–266. http://linkinghub.elsevier.com/retrieve/pii/S0034425796000673.

Garrity, S. R., C. D. Allen, S. P. Brumby, C. Gangodagamage, N. G. McDowell, and D. M. Cai. **2013**. Quantifying tree mortality in a mixed species woodland using multitemporal high spatial resolution satellite imagery. Remote Sensing of Environment 129:54–65. http://dx.doi.org/10.1016/j.rse.2012.10.029.

Gaylord, M. L., T. E. Kolb, W. T. Pockman, J. A. Plaut, E. A. Yepez, A. K. Macalady, R. E. Pangle, and N. G. McDowell. **2013**. Drought predisposes piñon-juniper woodlands to insect attacks and mortality. New Phytologist 198:567–578. http://doi.wiley.com/10.1111/nph.12174.

Google Earth Engine Team, **2015**. Google Earth Engine: A planetary-scale geo-spatial analysis platform. https://earthengine.google.com.

Gottfried, G. J., T. W. Swetnam, C. D. Allen, J. L. Betancourt, and A. L. Chung-MacCoubrey, **1995**. Pinyon-Juniper Woodlands. Chapter 6, page 186 *in* D. M. Finch and J. A. Tainter, editors. Ecology, Diversity, and Sustainability of the Middle Rio Grande Basin. General Technical Report RM-GTR-268.

Fort Collins, Colorado. https://www.fs.fed.us/rmrs/publications/ecology-diversity-and-sustainability-middle-rio-grande-basin.

Haibo He, and E. Garcia. **2009**. Learning from Imbalanced Data. IEEE Transactions on Knowledge and Data Engineering 21:1263–1284. http://ieeexplore.ieee.org/document/5128907/.

Hansen, M. C., P. V. Potapov, R. Moore, M. Hancher, S. A. Turubanova, A. Tyukavina, D. Thau, S. V. Stehman, S. J. Goetz, T. R. Loveland, A. Kommareddy, A. Egorov, L. Chini, C. O. Justice, and J. R. G. Townshend. **2013**. High-Resolution Global Maps of 21st-Century Forest Cover Change. Science 342:850–853. http://science.sciencemag.org/content/342/6160/850.

Hanson, P. J., and J. F. Weltzin. **2000**. Drought disturbance from climate change: response of United States forests. Science of The Total Environment 262:205–220. http://linkinghub.elsevier.com/retrieve/pii/S0048969700005234.

Hart, S. J., and T. T. Veblen. **2015**. Detection of spruce beetle-induced tree mortality using high- and medium-resolution remotely sensed imagery. Remote Sensing of Environment 168:134–145. http://linkinghub.elsevier.com/retrieve/pii/S0034425715300456.

Hartmann, H., H. D. Adams, W. R. L. Anderegg, S. Jansen, and M. J. B. Zeppel. **2015**. Research frontiers in drought-induced tree mortality: Crossing scales and disciplines. New Phytologist 205:965–969. http://dx.doi.org/10.1111/nph.13246.

Healey, S. P., W. B. Cohen, Y. Zhiqiang, and O. N. Krankina. **2005**. Comparison of Tasseled Cap-based Landsat data structures for use in forest disturbance detection. Remote Sensing of Environment 97:301–310. http://dx.doi.org/10.1016/j.rse.2005.05.009.

Hicke, J. A., C. D. Allen, A. R. Desai, M. C. Dietze, R. J. Hall, E. H. (Ted) Hogg, D. M. Kashian, D. Moore, K. F. Raffa, R. N. Sturrock, and J. Vogelmann. **2012***a*. Effects of biotic disturbances on forest carbon cycling in the United States and Canada. Global Change Biology 18:7–34. http://doi.wiley.com/10.1111/j.1365-2486.2011.02543.x.

Hicke, J. A., M. C. Johnson, J. L. Hayes, and H. K. Preisler. **2012***b*. Effects of bark beetle-caused tree mortality on wildfire. Forest Ecology and Management 271:81–90. http://dx.doi.org/10.1016/j.foreco.2012.02.005.

Hicke, J. A., and J. Logan. **2009**. Mapping whitebark pine mortality caused by a mountain pine beetle outbreak with high spatial resolution satellite imagery. International Journal of Remote Sensing 30:4427–4441. http://www.tandfonline.com/doi/abs/10.1080/01431160802566439.

Hicke, J. A., and M. J. B. Zeppel. **2013**. Commentary: Climate-driven tree mortality: insights from the piñon pine die-off in the United States. New Phytologist 200:301–303. http://doi.wiley.com/10.1111/nph.12464.

Homer, C., J. Dewitz, L. Yang, S. Jin, P. Danielson, G. Xian, J. Coulston, N. Herold, J. Wickham, and K. Megown. **2015**. Completion of the 2011 National Land Cover Database for the conterminous United States-Representing a decade of land cover change information. Photogrammetric Engineering and Remote Sensing 81:345–354.

Huang, C. Y., G. P. Asner, N. N. Barger, J. C. Neff, and M. L. Floyd. **2010**. Regional aboveground live carbon losses due to drought-induced tree dieback in piñon-juniper ecosystems. Remote Sensing of Environment 114:1471–1479. http://dx.doi.org/10.1016/j.rse.2010.02.003.

Huete, A. **1988**. A soil-adjusted vegetation index (SAVI). Remote Sensing of Environment 25:295–309. http://linkinghub.elsevier.com/retrieve/pii/003442578890106X.

Hurteau, M. D., J. B. Bradford, P. Z. Fulé, A. H. Taylor, and K. L. Martin. **2014**. Climate change, fire management, and ecological services in the southwestern US. Forest Ecology and Management 327:280–289. http://dx.doi.org/10.1016/j.foreco.2013.08.007.

IPCC. **2014**a. Climate Change 2014: Synthesis Report. Contribution of Working Groups I, II and III to the Fifth Assessment Report of the Intergovernmental Panel on Climate Change. Geneva, Switzerland.

IPCC, **2014**b. Summary for policymakers. Pages 1–32 in C. Field, V. Barros, D. Dokken, K. Mach, M. Mastrandrea, T. Bilir, M. Chatterjee, K. Ebi, Y. Estrada, R. Genova, B. Girma, E. Kissel, A. Levy, S. MacCracken, P. Mastrandrea, and L. White, editors. Climate Change 2014: Impacts, Adaptation, and Vulnerability. Part A: Global and Sectoral Aspects. Contribution of Working Group II to the Fifth Assessment Report of the Intergovernmental Panel on Climate Change. Cambridge University Press, Cambridge, United Kingdom and New York, NY, USA.

Jarvis, A., H. I. Reuter, A. Nelson, and E. Guevara, **2008**. Hole-filled seamless SRTM data Version 4, International Centre for Tropical Agriculture (CIAT). http://srtm.csi.cgiar.org.

Jensen, J. R. **2007**. Remote Sensing of the Environment: An Earth Resource Perspective. Second ed edition. Pearson Education.

Karl, T. R., J. M. Melillo, and T. C. Peterson, editors. **2009**. Global Climate Change Impacts in the United States. U.S. Global Change Research Program. Cambridge University Press. http://www.cambridge.org/9780521144070.

Korhonen, L., K. Korhonen, P. Stenberg, M. Maltamo, and M. Rautiainen. **2007**. Local models for forest canopy cover with beta regression. Silva Fennica 41:671–685. http://www.silvafennica.fi/article/275.

Krofcheck, D. J., J. U. Eitel, L. A. Vierling, U. Schulthess, T. M. Hilton, E. Dettweiler-Robinson, R. Pendleton, and M. E. Litvak. **2014**. Detecting mortality induced structural and functional changes in a piñon-juniper woodland using Landsat and RapidEye time series. Remote Sensing of Environment 151:102–113. http://linkinghub.elsevier.com/retrieve/pii/S0034425713004203.

Lanner, R. M. **1981**. The Piñon Pine: A Natural and Cultural History. University of Nevada Press, Reno, Nevada. https://books.google.com/books?id=u37wAAAAMAAJ.

Lawrimore, J., and S. Stephens. **2003**. Climate of 2002 Annual Review. NOAA National Climatic Data Center ftp://ftp.ncdc.noaa.gov/pub/data/extremeevents/specialreports/Climate-of-2002-Annaul_Review.pdf.

Liaw, A., and M. Wiener. **2002**. Classification and Regression by randomForest. R News 2:18–22.

Long, J. A., and R. L. Lawrence. **2016**. Mapping Percent Tree Mortality Due to Mountain Pine Beetle Damage. Forest Science 62:392–402. https://doi.org/10.5849/forsci.15-046.

Lutes, D. C., R. E. Keane, J. F. Caratti, C. H. Key, N. C. Benson, S. Sutherland, and L. J. Gangi, **2006**. FIREMON: Fire effects monitoring and inventory system. Gen. Tech. Rep. USDA Forest Service RMRS-GTR-164-CD. Technical Report June, Fort Collins, CO, USA. https://treesearch.fs.fed.us/pubs/24042.

Masek, J., E. Vermote, N. Saleous, R. Wolfe, F. Hall, K. Huemmrich, F. Gao, J. Kutler, and T.-K. Lim. **2006**. A Landsat Surface Reflectance Dataset for North America, 1990–2000. IEEE Geoscience and Remote Sensing Letters 3:68–72. http://dx.doi.org/10.1109/LGRS.2005.857030.

McCarley, T. R., C. A. Kolden, N. M. Vaillant, A. T. Hudak, A. M. Smith, B. M. Wing, B. S. Kellogg, and J. Kreitler. **2017**. Multi-temporal LiDAR and Landsat quantification of fire-induced changes to forest structure. Remote Sensing of Environment http://linkinghub.elsevier.com/retrieve/pii/S0034425716305016.

McDowell, N., W. T. Pockman, C. D. Allen, D. D. Breshears, N. Cobb, T. Kolb, J. Plaut, J. Sperry, A. West, D. G. Williams, and E. a. Yepez. **2008**. Mechanisms of plant survival and mortality during drought: Why do some plants survive while others succumb to drought? New Phytologist 178:719–739. doi.wiley.com/10.1111/j.1469-8137.2008.02436.x.

McDowell, N. G. **2011**. Mechanisms linking drought, hydraulics, carbon metabolism, and vegetation mortality. Plant physiology 155:1051–1059. http://dx.doi.org/10.1104/pp.110.170704.

McDowell, N. G., D. J. Beerling, D. D. Breshears, R. A. Fisher, K. F. Raffa, and M. Stitt. **2011**. The interdependence of mechanisms underlying climate-driven vegetation mortality. Trends in Ecology & Evolution 26:523–532. http://linkinghub.elsevier.com/retrieve/pii/S0169534711001698.

McDowell, N. G., N. C. Coops, P. S. Beck, J. Q. Chambers, C. Gangodagamage, J. A. Hicke, C.-y. Huang, R. Kennedy, D. J. Krofcheck, M. Litvak, A. J. Meddens, J. Muss, R. Negrón-Juarez, C. Peng, A. M. Schwantes, J. J. Swenson, L. J. Vernon, A. P. Williams, C. Xu, M. Zhao, S. W. Running, and C. D. Allen. **2015***a*. Global satellite monitoring of climate-induced vegetation disturbances. Trends in Plant Science 20:114–123. http://linkinghub.elsevier.com/retrieve/pii/S1360138514002726.

McDowell, N. G., A. P. Williams, C. Xu, W. T. Pockman, L. T. Dickman, S. Sevanto, R. Pangle, J.-M. Limousin, J. Plaut, D. S. Mackay, J. Ogee, J. C. Domec, C. D. Allen, R. A. Fisher, X. Jiang, J. D. Muss, D. D. Breshears, S. A. Rauscher, and C. Koven. **2015***b*. Multi-scale predictions of massive conifer mortality due to chronic temperature rise. Nature Climate Change 6:295–300. http://www.nature.com/doifinder/10.1038/nclimate2873.

Meddens, A., J. Hicke, and B. Jacobs. **2016**. Characterizing the Response of Piñon-Juniper Woodlands to Mechanical Restoration Using High-Resolution Satellite Imagery. Rangeland Ecology & Management 69:215–223. http://www.sciencedirect.com/science/article/pii/S1550742415001736.

Meddens, A. J., J. A. Hicke, and L. A. Vierling. **2011**. Evaluating the potential of multispectral imagery to map multiple stages of tree mortality. Remote Sensing of Environment 115:1632–1642. http://dx.doi.org/10.1016/j.rse.2011.02.018.

Meddens, A. J., J. A. Hicke, L. A. Vierling, and A. T. Hudak. **2013**. Evaluating methods to detect bark beetle-caused tree mortality using single-date and multi-date Landsat imagery. Remote Sensing of Environment 132:49–58. http://linkinghub.elsevier.com/retrieve/pii/S0034425713000060.

Meddens, A. J. H., and J. A. Hicke. **2014**. Spatial and temporal patterns of Landsat-based detection of tree mortality caused by a mountain pine beetle outbreak in Colorado, USA. Forest Ecology and Management 322:78–88. http://dx.doi.org/10.1016/j.foreco.2014.02.037.

Meddens, A. J. H., J. A. Hicke, and C. A. Ferguson. **2012**. Spatiotemporal patterns of observed bark beetle-caused tree mortality in British Columbia and the western

United States. Ecological Applications 22:1876–1891. http://doi.wiley.com/10.1890/11-1785.1.

Meddens, A. J. H., J. A. Hicke, A. K. Macalady, P. C. Buotte, T. R. Cowles, and C. D. Allen. **2015**. Tansley insight: Patterns and causes of observed piñon pine mortality in the southwestern United States. New Phytologist 206:91–97. http://doi.wiley.com/10.1111/nph.13193.

Meddens, A. J. H., J. A. Hicke, L. A. Vierling, and J. U. H. Eitel, **2009**. Detection of Beetle-Caused Tree Mortality from Satellite Imagery for Use in the LANDFIRE Project: Methods Development and Evaluation. Technical report.

Meigs, G. W., R. E. Kennedy, and W. B. Cohen. **2011**. A Landsat time series approach to characterize bark beetle and defoliator impacts on tree mortality and surface fuels in conifer forests. Remote Sensing of Environment 115:3707–3718. http://linkinghub.elsevier.com/retrieve/pii/S0034425711003361.

Melillo, J. M., T. Richmond, and G. W. Yohe, editors. **2014**. Climate Change Impacts in the United States: The Third National Climate Assessment. U.S. Global Change Research Program.

Moran, A. P. A. P. **1950**. Notes on Continuous Stochastic Phenomena. Biometrika 37:17–23. http://www.jstor.org/stable/2332142.

NOAA, **2016**. DROUGHT: Monitoring Economic, Environmental, and Social Impacts. National Oceanic and Atmospheric Administration. https://www.ncdc.noaa.gov/news/drought-monitoring-economic-environmental-and-social-impacts.

Oreskes, N. **2004**. Beyond The Ivory Tower: The Scientific Consensus on Climate Change. Science 306:1686–1686. http://www.sciencemag.org/cgi/doi/10.1126/science.1103618.

Ospina, R., and S. L. Ferrari. **2012**. A general class of zero-or-one inflated beta regression models. Computational Statistics & Data Analysis 56:1609–1623. http://dx.doi.org/10.1016/j.csda.2011.10.005.

Ospina, R., and S. L. P. Ferrari. **2010**. Inflated beta distributions. Statistical Papers 51:111–126. http://link.springer.com/10.1007/s00362-008-0125-4.

Perry, D. A., R. Oren, and S. C. Hart. **2008**. Forest Ecosystems. Second edition. The Johns Hopkins University Press, Baltimore, Maryland.

Pons, X., L. Pesquer, J. Cristóbal, and O. González-Guerrero. **2014**. Automatic and improved radiometric correction of Landsat imagery using reference values from MODIS surface reflectance images. International Journal of Applied Earth

Observation and Geoinformation 33:243–254. http://linkinghub.elsevier.com/retrieve/pii/S0303243414001354.

R Core Team, **2016**. R: A Language and Environment for Statistical Computing. R Foundation for Statistical Computing, Vienna, Austria. https://www.R-project.org.

Raffa, K. F., B. H. Aukema, B. J. Bentz, A. L. Carroll, J. A. Hicke, M. G. Turner, and W. H. Romme. **2008**. Cross-scale Drivers of Natural Disturbances Prone to Anthropogenic Amplification: The Dynamics of Bark Beetle Eruptions. BioScience 58:501.

Redmond, K. T. **2002**. The Depiction of Drought: A Commentary. Bulletin of the American Meteorological Society 83:1143–1147. http://dx.doi.org/10.1175/1520-0477(2002)083%3C1143:TDODAC%3E2.3.CO;2.

Rigby, R. A., and D. M. Stasinopoulos. **2005**. Generalized additive models for location, scale and shape (with discussion). Journal of the Royal Statistical Society: Series C (Applied Statistics) 54:507–554. http://doi.wiley.com/10.1111/j.1467-9876.2005.00510.x.

Roberts, D., M. Gardner, R. Church, S. Ustin, G. Scheer, and R. Green. **1998**. Mapping Chaparral in the Santa Monica Mountains Using Multiple Endmember Spectral Mixture Models. Remote Sensing of Environment 65:267 – 279. http://www.sciencedirect.com/science/article/pii/S0034425798000376.

Rock, B. N., J. E. Vogelmann, D. L. Williams, A. F. Vogelmann, and T. Hoshizaki. **1986**. Remote Detection of Forest Damage. BioScience 36:439–445. http://www.jstor.org/stable/info/10.2307/1310339.

Savage, S. L., R. L. Lawrence, and J. R. Squires. **2015**. Predicting relative species composition within mixed conifer forest pixels using zero-inflated models and Landsat imagery. Remote Sensing of Environment 171:326–336. http://dx.doi.org/10.1016/j.rse.2015.10.013.

Schwantes, A. M., J. J. Swenson, and R. B. Jackson. **2016**. Quantifying drought-induced tree mortality in the open canopy woodlands of central Texas. Remote Sensing of Environment 181:54–64. http://linkinghub.elsevier.com/retrieve/pii/S0034425716301213.

Sevanto, S., N. G. McDowell, L. T. Dickman, R. Pangle, and W. T. Pockman. **2014**. How do trees die? A test of the hydraulic failure and carbon starvation hypotheses. Plant, cell & environment 37:153–61. http://doi.wiley.com/10.1111/pce.12141.

Shaw, J. D., B. E. Steed, and L. T. DeBlander. **2005**. Forest inventory and analysis (FIA) annual inventory answers the question: What is happening to pinyon-juniper woodlands? Journal of Forestry 103:280–285.

Somers, B., G. P. Asner, L. Tits, and P. Coppin. **2011**. Endmember variability in Spectral Mixture Analysis: A review. Remote Sensing of Environment 115:1603–1616. http://linkinghub.elsevier.com/retrieve/pii/S0034425711000800.

Symonds, M. R. E., and A. Moussalli. **2011**. A brief guide to model selection, multimodel inference and model averaging in behavioural ecology using Akaike's information criterion. Behavioral Ecology and Sociobiology 65:13–21. http://link.springer.com/10.1007/s00265-010-1037-6.

Tucker, C. **1979**. Red and photographic infrared linear combinations for monitoring vegetation. Remote Sensing of Environment 8:127–150. http://dx.doi.org/10.1016/0034-4257(79)90013-0.

USGS, **2011**. National Gap Analysis Program (GAP), Land Cover Data, Version 2. http://gapanalysis.usgs.gov/gaplandcover/.

USGS, **2016**. Product Guide: Landsat 4-7 Climate Data Record (CDR) Surface Reflectance. Technical report, U.S. Department of the Interior/U.S. Geological Survey.

Vuolo, F., M. Mattiuzzi, and C. Atzberger. **2015**. Comparison of the Landsat Surface Reflectance Climate Data Record (CDR) and manually atmospherically corrected data in a semi-arid European study area. International Journal of Applied Earth Observation and Geoinformation 42:1–10. http://dx.doi.org/10.1016/j.jag.2015.05.003.

Warnock, D. D., M. E. Litvak, L. Morillas, and R. L. Sinsabaugh. **2016**. Drought-induced pinyon mortality alters the seasonal dynamics of microbial activity in pinyon-juniper woodland. Soil Biology and Biochemistry 92:91–101. http://dx.doi.org/10.1016/j.soilbio.2015.09.007.

Wilhite, D. A., and M. Buchanan-Smith. **2005**. Drought as a Hazard: Understanding the Natural and Social Context.

Wilhite, D. A., and M. H. Glantz. **1985**. Understanding the Drought Phenomenon: The Role of Definitions. Water International 10:111–120. http://www.tandfonline.com/doi/abs/10.1080/02508068508686328.

Williams, A. P., C. D. Allen, A. K. Macalady, D. Griffin, C. A. Woodhouse, D. M. Meko, T. W. Swetnam, S. a. Rauscher, R. Seager, H. D. Grissino-Mayer, J. S. Dean, E. R. Cook, C. Gangodagamage, M. Cai, and N. G. McDowell. **2012**. Temperature as a potent driver of regional forest drought stress and tree mortality. Nature Climate Change 3:292–297. http://dx.doi.org/10.1038/nclimate1693.

Willmott, C., and K. Matsuura. **2005**. Advantages of the mean absolute error (MAE) over the root mean square error (RMSE) in assessing average model performance. Climate Research 30:79–82. http://www.int-res.com/abstracts/cr/v30/n1/p79-82/.

Wing, B. M., M. W. Ritchie, K. Boston, W. B. Cohen, A. Gitelman, and M. J. Olsen. **2012**. Prediction of understory vegetation cover with airborne lidar in an interior ponderosa pine forest. Remote Sensing of Environment 124:730–741. http://dx.doi.org/10.1016/j.rse.2012.06.024.

Wright, M. N., and A. Ziegler. **2015**. ranger: A Fast Implementation of Random Forests for High Dimensional Data in C++ and R. arXiv.org stat.ML. http://arxiv.org/abs/1508.04409.

Wulder, M. A., C. C. Dymond, J. C. White, D. G. Leckie, and A. L. Carroll. **2006**. Surveying mountain pine beetle damage of forests: A review of remote sensing opportunities. Forest Ecology and Management 221:27–41. http://linkinghub.elsevier.com/retrieve/pii/S0378112705005736.

Zhang, Y., C. Peng, W. Li, and X. Fang. **2013**. Estimating Drought-Induced Impacts on Forest Structure, Growth, Function, and Ecosystem Services Using Remote-Sensing Data: Recent Progress and Future Challenges. Environmental Review 115:103–115. http://www.nrcresearchpress.com/doi/abs/10.1139/er-2013-0006.

Zhu, Z., and C. E. Woodcock. **2012**. Object-based cloud and cloud shadow detection in Landsat imagery. Remote Sensing of Environment 118:83–94. http://dx.doi.org/10.1016/j.rse.2011.10.028.

Appendix A. Additional analyses and statistical methods tested

Additional analyses and statistical methods tested. Comments relative to final model used in this study.

| Model framework	Method or analysis	Comment
ZIB	Added nonlinear smoothing functions to model predictors	Increased computational time significantly, thus did not pursue further
ZIB	Temporally smoothed NDWI′ using a per-pixel three-year running mean, then ran a bivariate model using the smoothed NDWI′ to predict PTM	No significant improvement to model performance
ZIB	Included a function of pixel UTM coordinates as an explanatory variable	Increased model performance, but model could not be applied outside the geographic region of the reference data
ZIB, RF	Pixels spatially sampled x meters apart from each other, where x was defined using the distance range estimated by semivariograms of model residuals	Similar accuracy metrics as those reported in this study, but with increased computational demand for application of multiple models to Landsat time series
ZIB, RF	Masked training data using various percent tree cover thresholds (10%, 20%, etc.) derived from aggregated reference data	Slight improvement to model performance, but modeling was limited by data availability to region of reference data
–	Investigated image-to-image (relative) radiometric variation for several bright and dark pseudo-invariant features (PIFs) within the study area (identified on-screen)	Variation was present within Landsat-derived time series (e.g., B2, TCB, and MSI) for selected PIFs, but magnitude of variation was low relative to the range of values across the study area and period for those Landsat-derived variables (Table 2.4)

ZIB, zero-inflated beta regression; RF, random forest; PTM, percent tree mortality

## Appendix B. Workflow of two-step random forest modeling approach
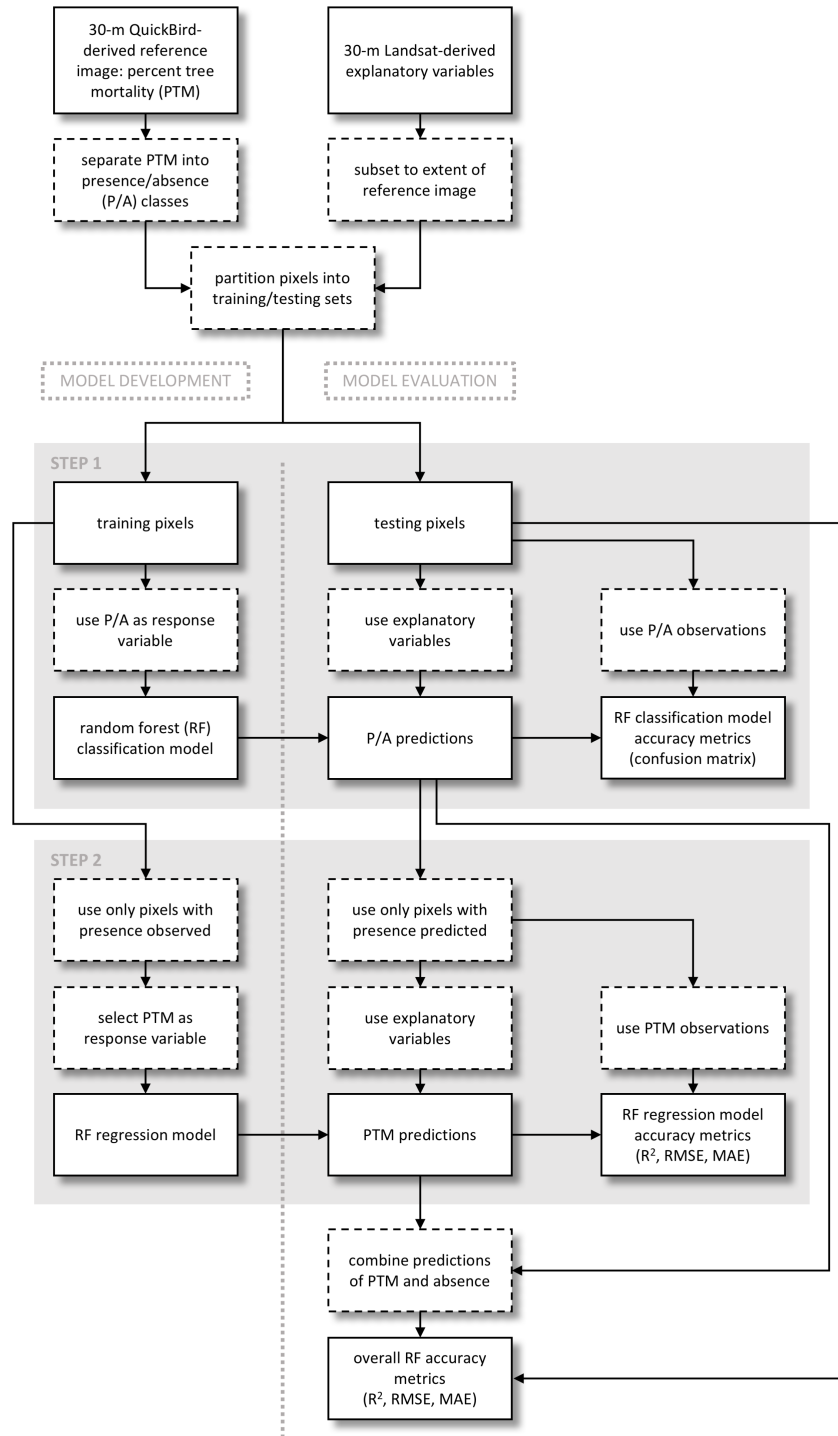
Workflow of the two-step random forest modeling approach used in this study. Boxes with solid outlines indicate products and boxes with dashed outlines indicate tasks.

# Appendix C. Correlation matrix for variables used in model development
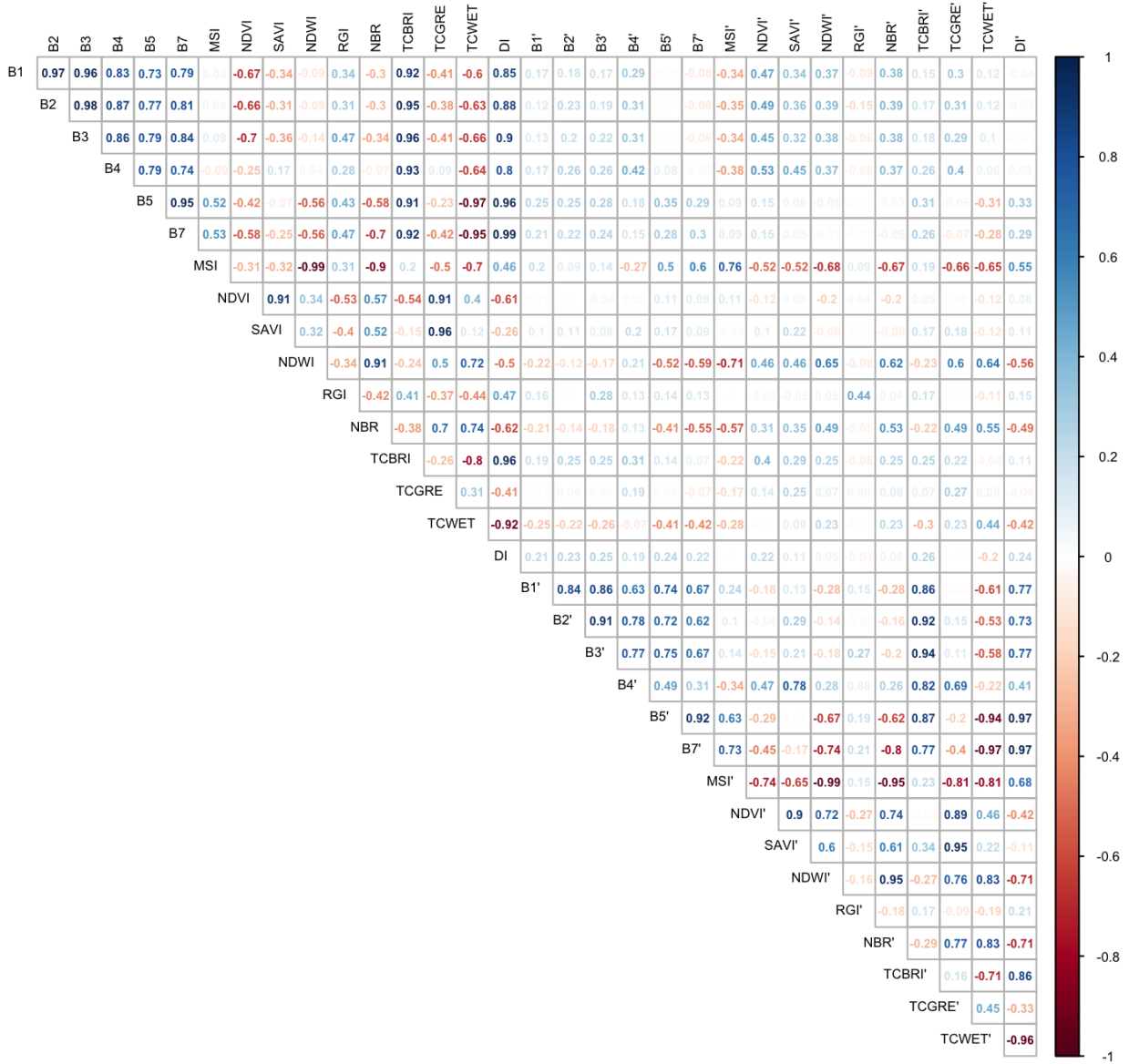
Correlation matrix used to determine correlation between all 32 candidate explanatory variables as indicated by the correlation coefficient (R). The explanatory variables are derived from 2006 Landsat imagery. Temporal anomalies ($'$) are calculated from a given variable's pre-drought (1990-99) per-pixel mean.

Appendix D. Variable importance plot for the balanced single-step RF model
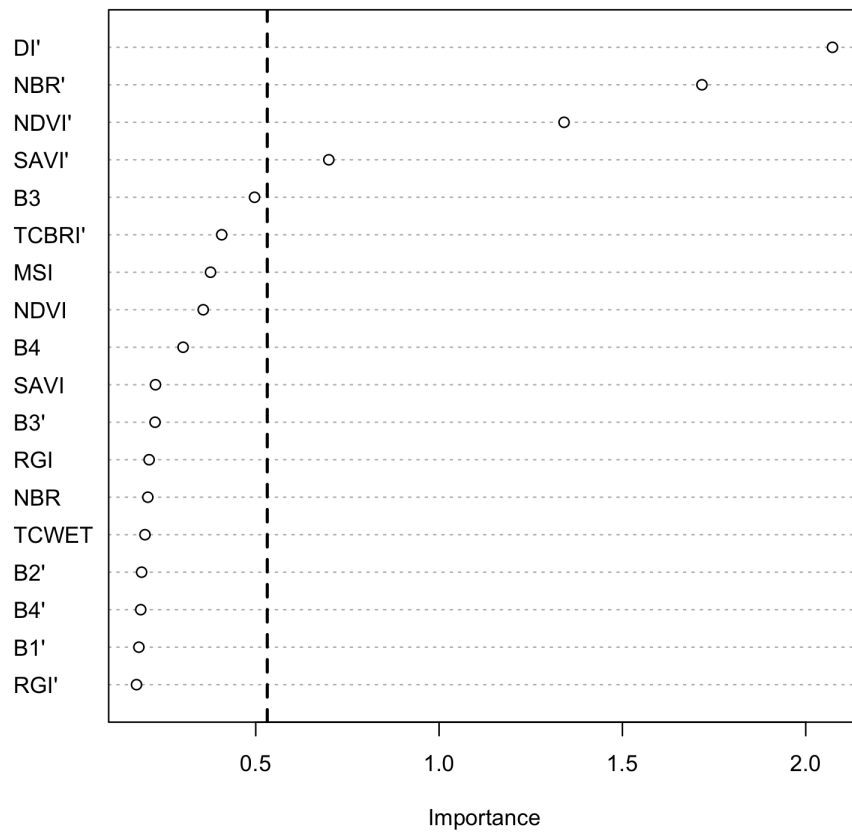
Variable importance (VI) plot using increase in node purity as the measure of VI for all non-redundant variables used in the balanced single-step RF model. The dashed black line indicates the mean VI. Temporal anomalies ($'$) were calculated from a 1990-99 per-pixel mean.

Appendix E. Frequency distributions of PTM used for unbalanced models
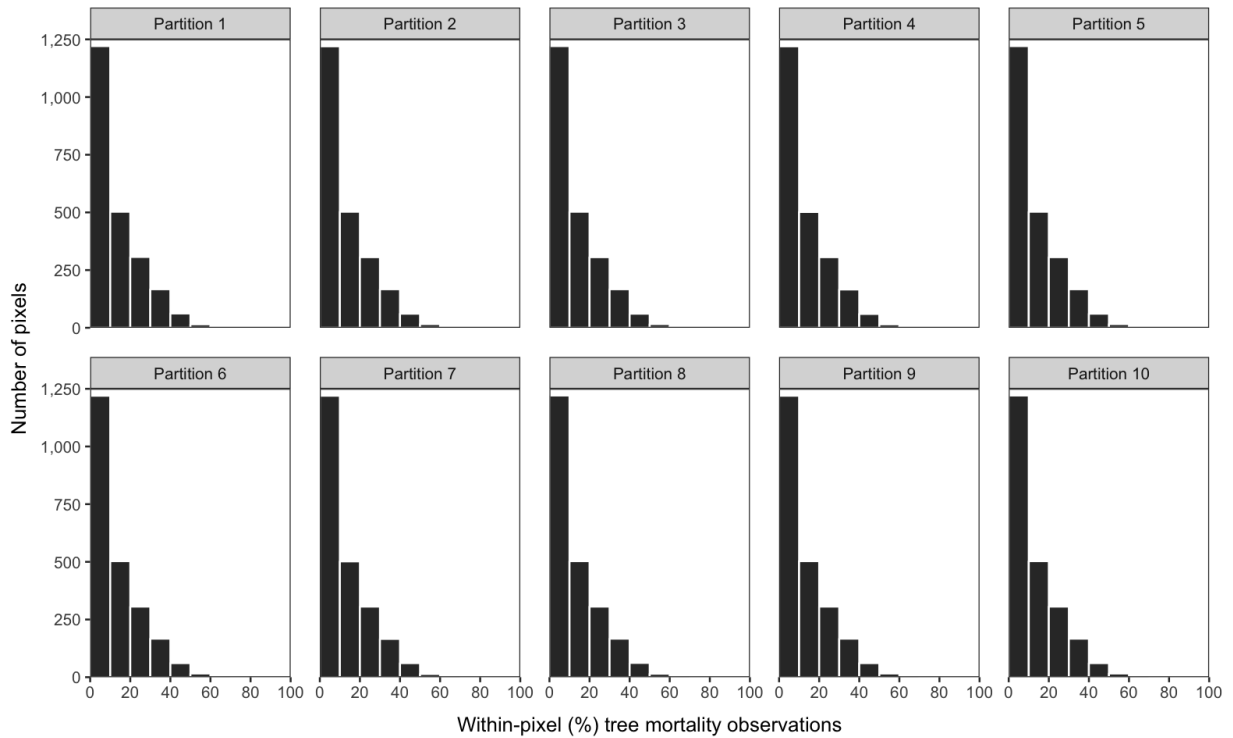
Frequency distributions across bins of percent mortality (within a 30-m grid cell) for partitions used during k-fold cross-validation ($k = 10$) to develop and evaluate unbalanced models.

Appendix F. Frequency distributions of PTM used for the balanced model
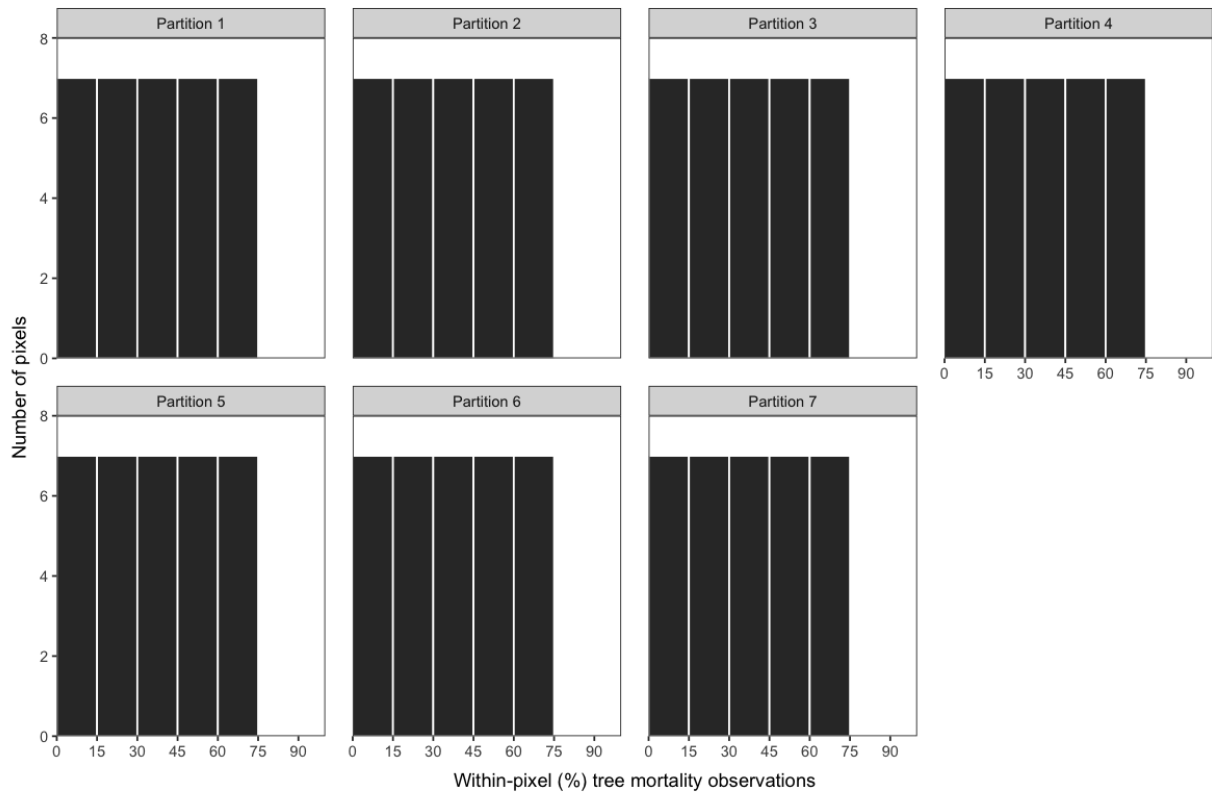
Frequency distributions across bins of percent mortality (within a 30-m grid cell) for partitions used during k-fold cross-validation ($k = 7$) to develop and evaluate the balanced random forest model.

Appendix G. Balanced RF model performance using 7-fold cross-validation

Comparison of precent tree mortality reference data and predictions for seven-times repeated model building and evaluation using the balanced single-step random forest model.

Fold	R^2	RMSE (%)	MAE (%)	ME (%)	Moran's I^a (p value)	N^b	N^c
1	0.48	15.64	10.52	-0.31	-0.042 (0.95)	210	35
2	0.65	13.01	10.39	-3.57	0.045 (0.72)	210	35
3	0.77	10.21	8.39	1.15	0.036 (0.76)	210	35
4	0.69	12.21	9.64	1.12	-0.029 (0.99)	210	35
5	0.57	14.40	12.19	0.48	-0.163 (0.52)	210	35
6	0.48	16.36	12.64	-0.01	0.041 (0.73)	210	35
7	0.79	10.13	7.99	1.24	0.302 (0.11)	210	35
Average across all folds	0.63	13.14	10.25	0.48	0.027 (0.69)	210	35

RMSE, root mean square error; MAE, mean absolute error; ME, mean error; N, number of samples.
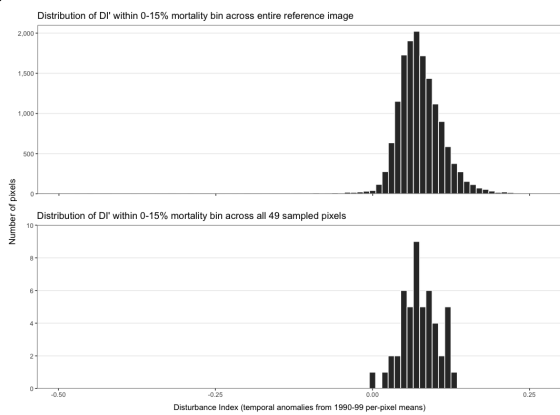
[a] Global Moran's I of the model residuals.
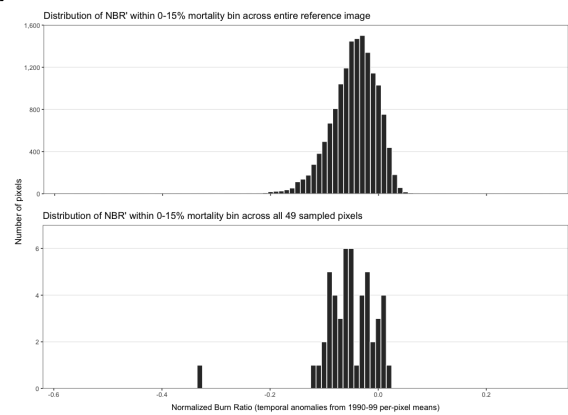
[b] Number of pixels sampled for model training.

[c] Number of pixels sampled for model testing.

Appendix H. Frequency distributions for explanatory variables used in the final model
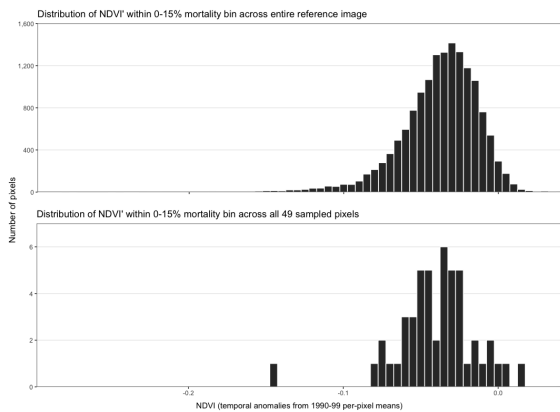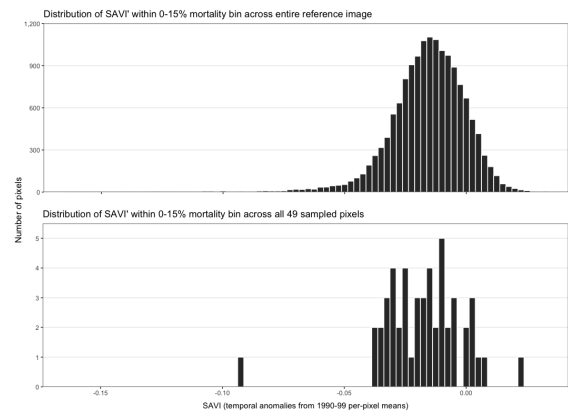

Frequency distributions of explanatory variables used in the final random forest model, including (A) DI′, (B) NBR′, (C) NDVI′, and (D) SAVI′, for the entire reference image (top panels) and the pixels sampled to create a balanced distribution of percent tree mortality for seven-times repeated model building and evaluation (bottom panels; $n = 49$).

Appendix I. Time series within the reference data region for various PTM thresholds
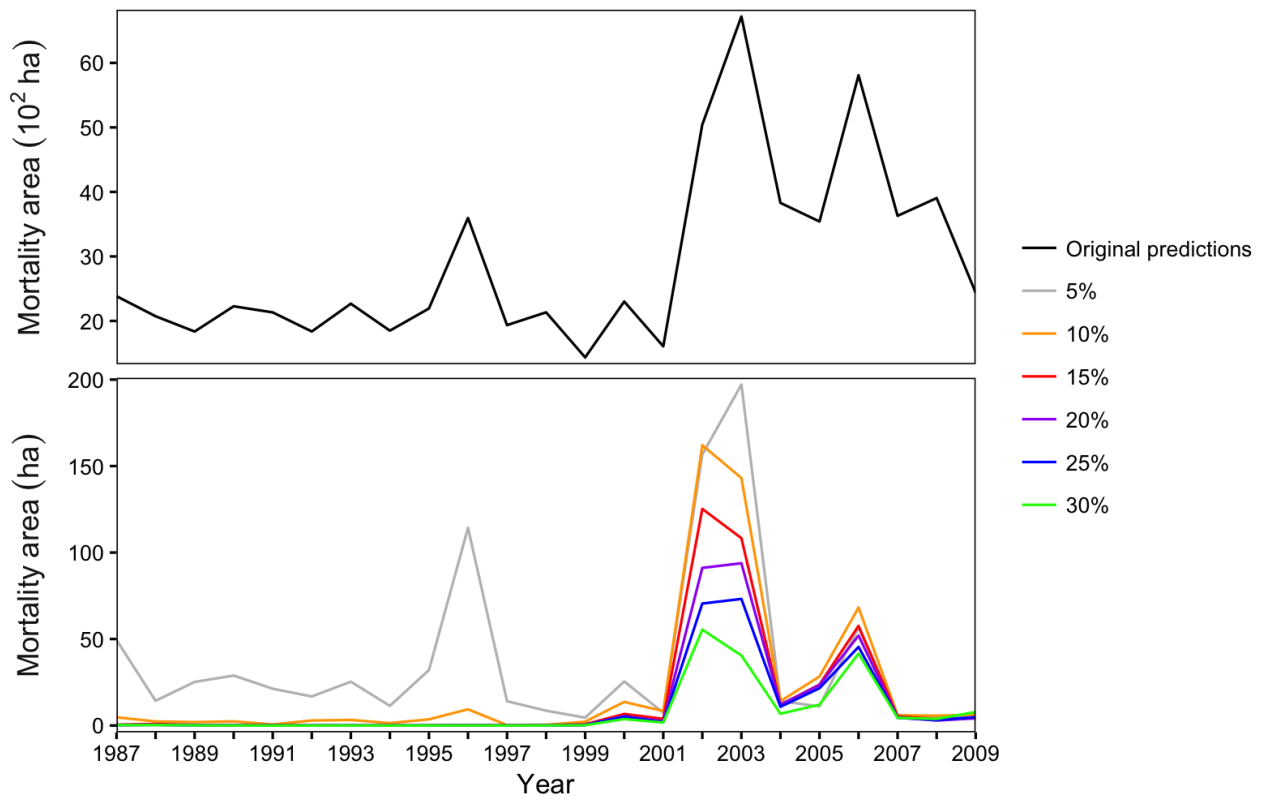
Time series of mortality area predictions from the final balanced single-step random forest model within the geographic extent of the reference data (top panel) and the post-processed mortality area time series using different thresholds (5%, 10%, ..., 30%) for reassigning low mortality severity predictions to 0% (bottom panel).

Appendix J. Time series of model predictions re-assigned to zero PTM
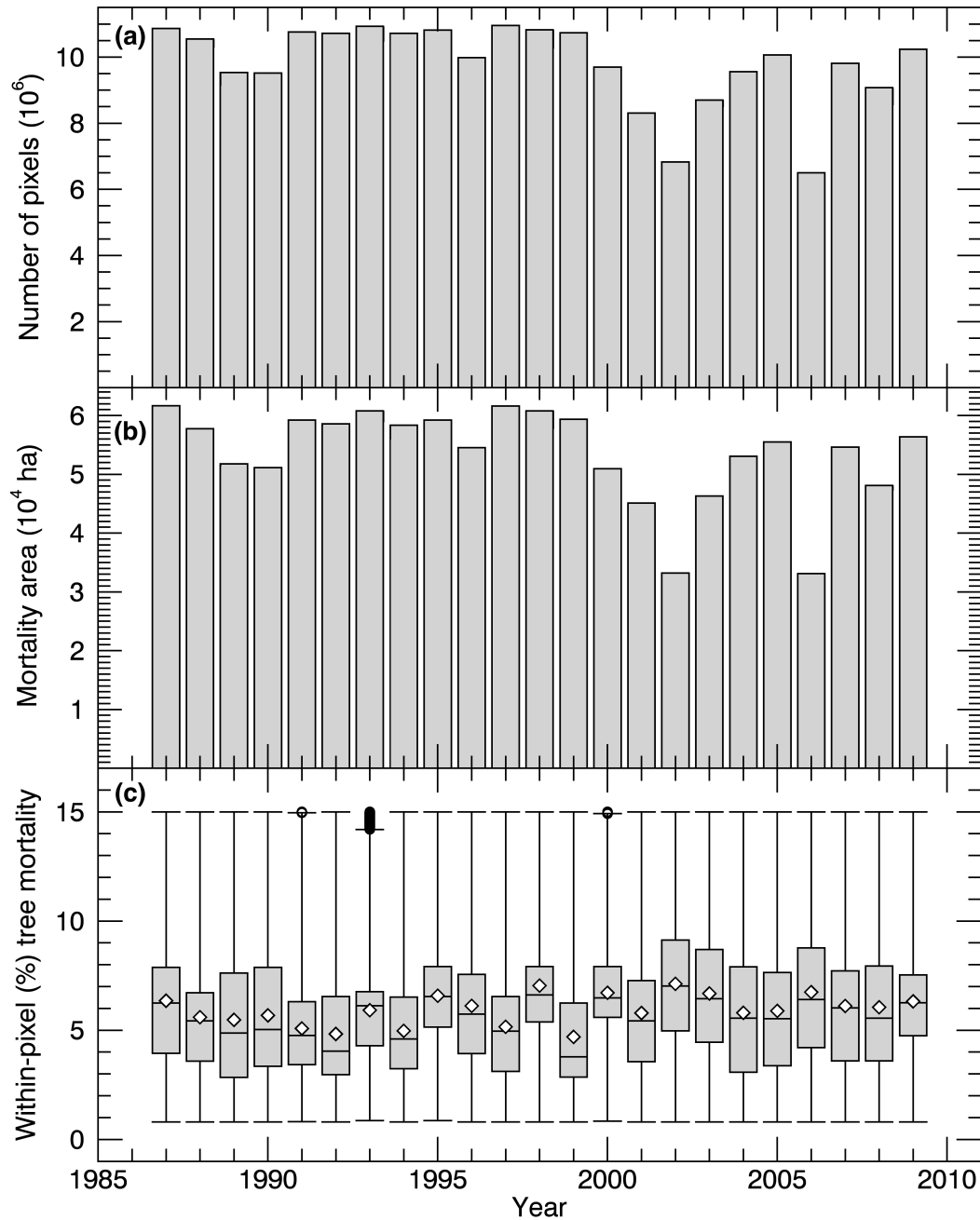
(a) The number of model predictions (pixels) per year re-assigned to zero PTM by applying a 15% mortality threshold, (b) the sum of mortality area (hectares) per year for those pixels, and (c) the distribution of PTM per year for those pixels. For (c), the horizontal line within the box indicates the median, the white diamond indicates the mean, boundaries of the gray box indicate the 25th- and 75th-percentile, the whiskers indicate the minimum and maximum PTM re-assigned to zero PTM per year, and circles indicate outliers.